Impact of scale dependent bias and nonlinear structure growth on the integrated Sachs-Wolfe effect: Angular power spectra

Smith, R E ; Hernandez-Monteagudo, C ; Seljak, U

Abstract: We investigate the impact of nonlinear evolution of the gravitational potentials in the LCDM model on the Integrated Sachs-Wolfe (ISW) contribution to the CMB temperature power spectrum, and on the cross-power spectrum of the CMB and a set of biased tracers of the mass. We use an ensemble of N-body simulations to directly follow the potentials and compare results to perturbation theory (PT). The predictions from PT match the results to high precision for k<0.2 h/Mpc. We compute the nonlinear corrections to the angular power spectrum and find them to be <10% of linear theory for l<100. These corrections are swamped by cosmic variance. On scales l>100 the departures are more significant, however the CMB signal is more than a factor 10^3 $larger at this scale. Nonlinear ISW effects therefore play no role in shaping the CMB po$ $1500. We analyze the CMB--density tracer cross-spectrum using simulations and renormalized bias PT, and find good agr$ $LSS cross-spectrum at small scales. However, PT analysis suggests that this trend reverses at late times when the logarithmi$ $d ln D/d ln a < 0.5 or o m_m(a) < 0.3. Numerical results confirm these expectations and we find no sign change in ISW-$ $LSS cross-power for low redshifts. Corrections due to nonlinearity and scale dependence of the bias are found to be <$ $10% for l < 100, therefore below the S/N of the current and future measurements. Finally, we estimate the CMB-$ $-halo cross-correlation coefficient and show that it can be made to match that for CMB--dark matter to within 5% for thinr$

DOI: https://doi.org/10.1103/PhysRevD.80.063528

Impact of Scale Dependent Bias and Nonlinear Structure Growth on Integrated Sachs-Wolfe Effect: Angular Power Spectra

Robert E. Smith
*Institute for Theoretical Physics, University of Zurich, Zurich CH 8037**

Carlos Hernández-Monteagudo
Max-Planck Institute For Astrophysics, P.O. Box 1523, 85741 Garching, Germany†

Uroš Seljak
Institute for Theoretical Physics, University of Zurich, Zurich CH 8037
Physics Department and Lawrence Berkeley National Laboratory,
University of California, Berkeley, California, 04720, USA. and
Ewha University, Seoul 120-750, S. Korea‡

We investigate the impact of nonlinear evolution of the gravitational potentials in the LCDM model on the Integrated Sachs-Wolfe (ISW) contribution to the CMB temperature power spectrum, and on the cross-power spectrum of the CMB and a set of biased tracers of the mass. We use an ensemble of N-body simulations to directly follow the potentials and compare the results to analytic perturbation theory (PT) methods. The predictions from the PT match the results to high precision for $k < 0.2\,h\,\mathrm{Mpc}^{-1}$. We compute the nonlinear corrections to the angular power spectrum and find them to be $< 10\%$ of linear theory for $l < 100$. These corrections are swamped by the cosmic variance. On scales $l > 100$ the departures are more significant, however the CMB signal is more than a factor 10^3 larger at this scale. Nonlinear ISW effects therefore play no role in shaping the CMB power spectrum for $l < 1500$. We analyze the CMB–density tracer cross-spectrum using simulations and renormalized bias PT, and find good agreement. The usual assumption is that nonlinear evolution enhances the growth of structure and counteracts the linear ISW on small scales, leading to a change in sign of the CMB-LSS cross-spectrum at small scales. However, PT analysis suggests that this trend reverses at late times when the logarithmic growth rate $f = d\ln D/d\ln a < 0.5$ or $\Omega_m(z) < 0.3$. Numerical results confirm these expectations and we find no sign change in ISW-LSS cross-power for low redshifts. Corrections due to nonlinearity and scale dependence of the bias are found to be $< 10\%$ for $l < 100$, therefore below the signal-to-noise of the current and future measurements. Finally, we estimate the cross-correlation coefficient between the CMB and halos and show that it can be made to match that for the dark matter and CMB to within 5% for thin redshift shells, thus mitigating the need to model bias evolution.

I. INTRODUCTION

Measurements of the temperature fluctuations in the Cosmic Microwave Background (CMB), provide a unique window onto the primordial Universe and a means to learn about the physical processes that generated the initial conditions. This discriminatory power is exemplified by recent results from the WMAP experiment [1]: the primordial power spectral index is $n_s = 0.960 \pm 0.013$, ruling out the Harrison-Zel'Dovich spectrum at 3σ level. However, the temperature power spectrum does not provide a pristine window, but it must be cleaned for the imprint of foreground signals. One cosmological foreground, is the change in energy that a CMB photon experiences as it propagates through an inhomogeneous Universe with time evolving gravitational potentials, $\dot{\Phi}$. There are three main effects that may give rise to such secondary fluctuations:

- Linear Integrated Sachs–Wolfe Effect[2, hereafter ISW]: unless the growth of density perturbations matches the expansion rate, $\dot{\Phi}$ will evolve from zero. This will lead to a net change in photon temperatures. In LCDM $|\dot{\Phi}| < 0$ as the potential decays, giving rise to a net positive correlation between density and temperature in Fourier space.

- Rees–Sciama Effect[3, hereafter RS]: nonlinear collapse of perturbations to filaments and clusters leads to $\dot{\Phi} \neq 0$ even in the absence of linear ISW, and CMB photons change energy as they transit across nonlinear structures. It is usually assumed that nonlinear evolution accelerates the growth of structure and counteracts the linear decay of gravitational potential in LCDM. In this paper we show that this is not always justified.

- Birkinshaw–Gull Effect[4, hereafter BG]: if a mass concentration moves transversely to the line of sight, it will create a time variation in the potential even if the potential itself is not evolving in time, and this will have a dipolar pattern. Consequently, photons which enter the potential in the wake, will

*Electronic address: res@physik.unizh.ch
†Electronic address: chm@MPA-Garching.MPG.DE
‡Electronic address: seljak@physik.unizh.ch

receive a net energy boost on exit, and those which enter ahead will loose energy on exit. However, unlike the previous two effects, this contributes only to the CMB auto-correlation and not to the cross-correlation of CMB with a density tracer.

All three effects combine into the nonlinear ISW. It is well known that the linear ISW effect leads to fluctuations of the order $\Delta T \approx 1\mu$K on the largest scales $l < 10$ for LCDM [see for example 5] and has been used to rule out the self-accelerating branch of DGP model [6].

The impact of the nonlinear evolution of $\dot{\Phi}$ on the CMB has been the subject of a number of studies. However, most of these works attempt to quantify the effect through the use of simplified analytic models [3, 7–12]. A number of studies have employed numerical simulations to track the evolution of $\dot{\Phi}$: in a pioneering study, Tuluie and Laguna [13] and Tuluie et al. [14] used ray tracing methods to compute the change in temperature for individual photon bundles propagating through inhomogeneous universes. They found that the combined imprint on the CMB power spectrum, due to the RS and BG effects, were of the order $\Delta T \sim 1\mu$K on angular scales $l \sim 200$. Owing to the limited size of their simulations, they were unable to comment on the effects on the lower multipoles. Seljak [15] related $\dot{\Phi}$ to density and momentum using the Poisson and continuity equation. These predictions were compared to an N-body simulation of the then favored SCDM model, and good agreement was found between the two as well as to those of Tuluie et al. [14]. However, these results were obtained in the context of $\Omega_m = 1$ model, where no linear ISW exists, and they could not address $l < 100$ behavior, owing to the limited dynamic range of the simulations. Puchades et al. [16] also recently addressed this problem, but again attention was focused on the large multipole regime.

In a more recent study, Cai et al. [17] used a single N-body simulation, the `L-BASIC` simulation, which has $N = 488^3$ and comoving length of $L = 1.34\,h^{-1}$Gpc, to compute the nonlinear ISW effect. They measured the $\dot{\Phi}$ power spectra at each epoch in the simulation and developed an empirical fitting formula for the deviations from linear theory. Using this model they computed the CMB angular power spectrum and found, on scales $l > 50$, that there was significant nonlinear amplification of power, qualitatively confirming the earlier halo model predictions of Cooray [11]. However, these nonlinear corrections occur on angular scales where the primary anisotropy spectrum is more than two orders of magnitude larger, rendering them of negligible importance. Cai et al. [17] also found that there was no evidence for deviations for multipoles $l < 50$. One of the aims of this paper is to place more precise constraints on the expected level of contamination on these large scales.

The temperature fluctuations induced through the evolving $\dot{\Phi}$ can also be observed by correlating the CMB against density perturbations, as pointed out by Crittenden and Turok [18], and the large-scale ISW effect provides an important test for Dark Energy and the curvature of the Universe. This information can be extracted through the cross-correlation of the CMB with tracers of the Large-Scale Structure (hereafter LSS). This analysis has recently been performed by a number of groups using the WMAP data and several large-scale structure measurements (e.g. SDSS, NVSS, 2MASS). This work has resulted in up to 4σ level detections of the ISW effect [19–27]. In the near future these detections will be improved upon with PLANCK and the new wide field LSS surveys, such as BOSS, DES, Pan-STARRS-1 and EUCLID, etc.. However, in a recent paper Granett et al. [28] measured the cross-correlation between superstructures and supervoids with the CMB. On stacking the signal they found a $\sim 4.5\sigma$ detection, in multiple WMAP bands, and the sign of which appeared consistent with late time ISW. This appears in stark contrast to expectations from simple signal-to-noise calculations within the LCDM model [18, 29–31]. A follow up 'consistency' test was performed by Granett et al. [32], the results of which cast some doubt on the the signal as arising from ISW, at least within the LCDM model. Cai et al. [17] also investigated the ISW-density cross-correlations, focusing on the nonlinearities arising from the mass evolution. They found that there was no evidence for enhancement of evolution of $\dot{\Phi}$, in agreement with the earlier work of Verde and Spergel [33]. One of the questions we shall address in this paper is whether selecting biased tracers of LSS relative to the mass distribution can influence the detection sensitivity for the ISW.

We pursue a two-pronged attack on all of these problems. Our first avenue will be to use a large ensemble of N-body simulations to directly follow the evolution of $\dot{\Phi}$. Our second line is analytic, and we use the nonlinear gravitational perturbation theory (PT) and renormalized bias frameworks to compute all measured quantities. This will help us to provide physical insight into the results along the way.

The paper breaks down as follows: In §II we summarize the basic theory of the ISW. In §III we describe the ensemble of simulations that we use, and describe our estimator for measuring $\dot{\Phi}$ from the simulations. Here we also present maps, comparing the time evolution of density, and $\dot{\Phi}$ in the simulations. In §IV we investigate the two-point statistics of $\dot{\Phi}$, and besides the usual linear analysis we derive nonlinear expressions within the context of the gravitational perturbation theory. We evaluate the theory and compare directly with measurements from the simulations. Then in §V we compute the impact on the CMB temperature power spectrum. In §VI we turn to the cross-correlations with dark matter, followed by the correlations with halos in §VII including the effects of scale dependent bias. Again, the theory is compared directly with measurements from the simulations. In §VIII we perform the line-of-sight integrals and compute angular cross-power spectra. Finally, in §IX we summarize our findings and conclude.

II. THEORETICAL BACKGROUND

A. The ISW effect

On arrival at the observer, the CMB photons, which are sourced at the surface of last scattering, $z \approx 1100$, are imprinted with two sets of fluctuations: the primary anisotropies, which are induced by the primordial fluctuations, perhaps seeded through the inflationary mechanism; and the secondary anisotropies, which are induced as the photons propagate through the clumpy Universe. The primary anisotropies have been studied in great detail for several decades[and for a review of the important processes see 5, 34]. There are a number of physical mechanisms that give rise to the generation of secondary anisotropies [for a review see 35] and one of these is the redshifting of the photons as they pass through evolving gravitational potentials.

The temperature fluctuation induced by the gravitational redshift may be written as [2]:

$$\frac{\Delta T(\hat{\mathbf{n}})}{T_0} = \frac{2}{c^2}\int_{t_{\rm ls}}^{t_0} dt \dot{\Phi}(\hat{\mathbf{n}}, \chi; t) \ , \tag{1}$$

where $\hat{\mathbf{n}}$ is a unit direction vector on the sphere, Φ is the dimensionless metric perturbation in the Newtonian gauge, which reduces to the usual gravitational potential on small scales, the 'over dot' denotes a partial derivative with respect to the coordinate time t from the FLRW metric, χ is the comoving radial geodesic distance $\chi = \int cdt/a(t)$, and so may equivalently parameterize time. t_0 and $t_{\rm ls}$ denote the time at which the photons are received and emitted (i.e. last scattering), respectively, c is the speed of light and $a(t)$ is the dimensionless scale factor.

On scales smaller than the horizon, the perturbed Poisson equation enables us to relate potential and matter fluctuations [36]:

$$\nabla^2\Phi(\mathbf{x}; t) = 4\pi G\bar{\rho}(t)\delta(\mathbf{x}; t)a^2(t) \ , \tag{2}$$

where $\bar{\rho}(t)$ is the mean matter density in the Universe and the density fluctuation is $\delta(\mathbf{x}; t) \equiv [\rho(\mathbf{x}, t) - \bar{\rho}(t)]/\bar{\rho}(t)$. Poisson's equation may most easily be solved in Fourier space, upon which we have,

$$\Phi(\mathbf{k}; t) = -4\pi G\bar{\rho}(t)a^2(t)\frac{\delta(\mathbf{k}; t)}{k^2} \ . \tag{3}$$

However, what we are really interested in is the instantaneous time rate of change of the potential,

$$\dot{\Phi}(\mathbf{k}; t) = -\frac{4\pi G}{k^2}\left[\bar{\rho}(t)a^3\right]\frac{\partial}{\partial t}\left[\frac{\delta(\mathbf{k}; t)}{a(t)}\right] \ , \tag{4}$$

$$= \frac{3}{2}\Omega_{m0}H_0^2k^{-2}\left[\frac{H(t)}{a(t)}\delta(\mathbf{k}; t) - \frac{\dot{\delta}(\mathbf{k}; t)}{a(t)}\right] \ , \tag{5}$$

where $[a^3(t)\bar{\rho}(t)]$ is a time independent quantity in the matter dominated epoch. In the above, we also defined $H(t) \equiv \dot{a}(t)/a(t)$ and $\Omega_m(t) \equiv \bar{\rho}(t)/\rho_{\rm crit}(t)$, with $\rho_{\rm crit}(t) = 3H^2(t)/8\pi G$. All quantities with a subscript 0 are to be evaluated at the present epoch. Estimating the change in the photon temperature due to the evolving potentials requires knowledge of the evolution of the density perturbation and its time rate of change. In the linear regime we may solve the equation of motion for δ exactly and obtain both of these quantities. However, in the nonlinear regime the situation is more complex and requires numerical simulations or nonlinear models to proceed. In simulations, measuring $\delta(\mathbf{k}, a)$ is relatively straightforward, whereas its time derivative is more complicated. As was shown by Seljak [15] one may obtain this from the perturbed continuity equation [36]:

$$\nabla\cdot\left[1 + \delta(\mathbf{x}; t)\right]\mathbf{v}_p(\mathbf{x}; t) = -a(t)\dot{\delta}(\mathbf{x}; t) \ , \tag{6}$$

where $\mathbf{v}_p(\mathbf{x}; t)$ is the proper peculiar velocity field. On defining the pseudo-peculiar momentum field to be,

$$\mathbf{p}(\mathbf{x}; t) \equiv \left[1 + \delta(\mathbf{x}; t)\right]\mathbf{v}_p(\mathbf{x}; t) \ , \tag{7}$$

then in Fourier space we may solve the continuity equation directly to give us:

$$\dot{\delta}(\mathbf{k}; t) = i\mathbf{k}\cdot\mathbf{p}(\mathbf{k}; t)/a(t) \ . \tag{8}$$

Hence, our final expression becomes,

$$\dot{\Phi}(\mathbf{k}; t) = \mathcal{F}(k)\left[\frac{H(t)}{a(t)}\delta(\mathbf{k}; t) - \frac{i\mathbf{k}\cdot\mathbf{p}(\mathbf{k}; t)}{a^2(t)}\right] \ , \tag{9}$$

where to enable us to pass easily from potential to density we introduced the quantity

$$\mathcal{F}(k) \equiv \frac{3}{2}\Omega_{m0}\left(\frac{H_0}{k^2}\right)^2 \ . \tag{10}$$

III. THE ISW FROM N-BODY SIMULATIONS

A. The zHORIZON simulations

In this study we use a subset of the Zürich Horizon, "zHORIZON", simulations. These are a large ensemble of pure cold dark matter N-body simulations ($N_{\rm sim} = 30$), performed at the University of Zürich on the zBOX2 and zBOX3 super-computers. The specific aim for these simulations is to provide high precision measurements of cosmic structures on scales of the order $\sim 100\,h^{-1}$Mpc and to also provide insight into the rarest fluctuations within the LCDM model that we should expect to find within the observable universe. In this paper we shall only employ the first 8 zHORIZON simulations, since these runs have 11 snapshots logarithmically spaced in the expansion factor from $z = 1$ to 0, thus giving sufficient time sampling of the simulated density field to capture the late time evolution. The expansion factors at which snapshots are recorded are: $a = \{1.0, 0.93, 0.87, 0.76, 0.66, 0.62, 0.57, 0.54, 0.5\}$.

Each numerical simulation was performed using the publicly available `Gadget-2` code [37], and followed the nonlinear evolution under gravity of $N = 750^3$ equal mass particles in a comoving cube of length $L = 1500\,h^{-1}$Mpc. All of the simulations were run within the same cosmological model, and the particular choice for the parameters was inspired by results from the WMAP experiment [1, 38, 39]. The parameters are: $\{\Omega_{m0} = 0.25,\, \Omega_{\rm DE,0} = 0.75, \Omega_{\rm b,0} = 0.04,\, \sigma_8 = 0.8,\, n_s = 1.0,\, w_0 = -1,\, h = 0.72\}$, where these are: the density parameters in matter, dark energy and baryons; the power spectrum normalization and primordial spectral index; equation of state parameter for dark energy $p/\rho = w_0$; dimensionless Hubble parameter. The transfer function for the simulations was generated using the publicly available `cmbfast` code [40, 41], with high sampling of the spatial frequencies on large scales. Initial conditions were lain down at redshift $z = 50$ using the serial version of the publicly available `2LPT` code [42, 43].

Dark matter halo catalogs were generated for all snapshots of each simulation using the Friends-of-Friends (FoF) algorithm [44], with the linking-length parameter set to the standard $b = 0.2$. For this we used the fast parallel `B-FoF` code, kindly provided by V. Springel. The minimum number of particles for which an object was considered to be a bound halo, was set to 30 particles. This gave a minimum host halo mass of $\sim 1.5 \times 10^{13} M_\odot/h$.

B. Estimating the ISW effect in simulations

In order to estimate $\dot\Phi$, we require estimates of both the density field and pseudo-peculiar momentum field in Fourier space (c.f. Eq. (9). The dark matter density field can be written as a sum over Dirac delta functions,

$$\rho(\mathbf{x}) = \sum_{l=1}^{N} m_l \delta^D(\mathbf{x} - \mathbf{x}_l) \ , \tag{11}$$

where m_l is the mass of the lth particle and we take all particles to have equal mass. The density field averaged on a cubical lattice can then be obtained through the convolution,

$$\begin{aligned} \rho_g(\mathbf{x}_{ijk}) &= \frac{1}{V_W} \int d^3x \rho(\mathbf{x}) W(\mathbf{x}_{ijk} - \mathbf{x}) \ ; \\ &= \frac{m}{V_\mu} \sum_l^N W(\mathbf{x}_{ijk} - \mathbf{x}_l) \ , \end{aligned} \tag{12}$$

where W represents the dimensionless window function of the mass assignment scheme, and where the normalization factor is $V_W = \int d^3x' W(\mathbf{x} - \mathbf{x}')$. The filter function W that we adopt throughout is the 'cloud-in-cell' charge assignment scheme [45]. Hence, our estimate for the density fluctuation is

$$\begin{aligned} 1 + \widehat{\delta(\mathbf{x})} &= \frac{1}{N} \frac{V_\mu}{V_W} \sum_l^N W(\mathbf{x}_{ijk} - \mathbf{x}_l) \ , \\ &= \frac{N_{\rm cell}}{N} \sum_l^N W(\mathbf{x}_{ijk} - \mathbf{x}_l) \ , \end{aligned} \tag{13}$$

where $N_{\rm cell} = V_\mu/V_W$ is the total number of grid cells.

The pseudo-momentum field may be estimated in a similar fashion. For convenience we write,

$$\mathbf{p} = [1 + \delta(\mathbf{x})]\, \mathbf{u}(\mathbf{x}) a(t) \ , \tag{14}$$

where $\mathbf{u} = \mathbf{v}_p/a$ is the comoving peculiar velocity field. The particle momentum field is then written as

$$[(1+\delta)\mathbf{u}]\,(\mathbf{x}) = \frac{V_\mu}{N} \sum_l^N \delta^D(\mathbf{x} - \mathbf{x}_l)\mathbf{u}_l \ . \tag{15}$$

This may be convolved with the mass assignment scheme to obtain the mesh averaged quantity

$$[(1+\delta)\mathbf{u}]\,(\mathbf{x}_{ijk}) = \frac{1}{N} \frac{V_\mu}{V_W} \sum_l^N \mathbf{u}_l W(\mathbf{x}_{ijk} - \mathbf{x}_l) \ . \tag{16}$$

Thus our estimate for the pseudo-momentum field is given by

$$\widehat{\mathbf{p}}(\mathbf{x}_{ijk}) = a(t) \frac{N_{\rm cell}}{N} \sum_l^N \mathbf{u}_l W(\mathbf{x}_{ijk} - \mathbf{x}_l) \ . \tag{17}$$

The density Fourier modes were then estimated using the publicly available `FFTW` routines [46], and each resulting mode was corrected for the convolution with the mass-assignment window function. For the CIC algorithm this corresponds to the following operation:

$$\delta_{\rm d}(\mathbf{k}) = \delta_{\rm g}(\mathbf{k}) / W_{\rm CIC}(\mathbf{k}) \ , \tag{18}$$

where

$$W_{\rm CIC}(\mathbf{k}) = \prod_{i=1,3} \left\{ \left[\frac{\sin\left[\pi k_i / 2k_{\rm Ny}\right]}{\left[\pi k_i / 2k_{\rm Ny}\right]} \right]^2 \right\} \tag{19}$$

and where sub-script d and g denote discrete and grid quantities, and where $k_{\rm Ny} = \pi N_{\rm g}/L$ is the Nyquist frequency, and $N_{\rm g}$ is the number of grid cells [45].

To obtain the real space $\dot\Phi(\mathbf{x}, t)$, we solved for $\dot\Phi(\mathbf{k}, t)$ in Fourier space using Eq. (9), set the unobservable $k = 0$ mode to zero, and inverse transformed back to real space.

C. Visual representation of the evolution of $\dot\Phi$

Fig. 1 shows how the dark matter particle number, projected in a slab of thickness $\Delta x = 100\,h^{-1}$Mpc and side

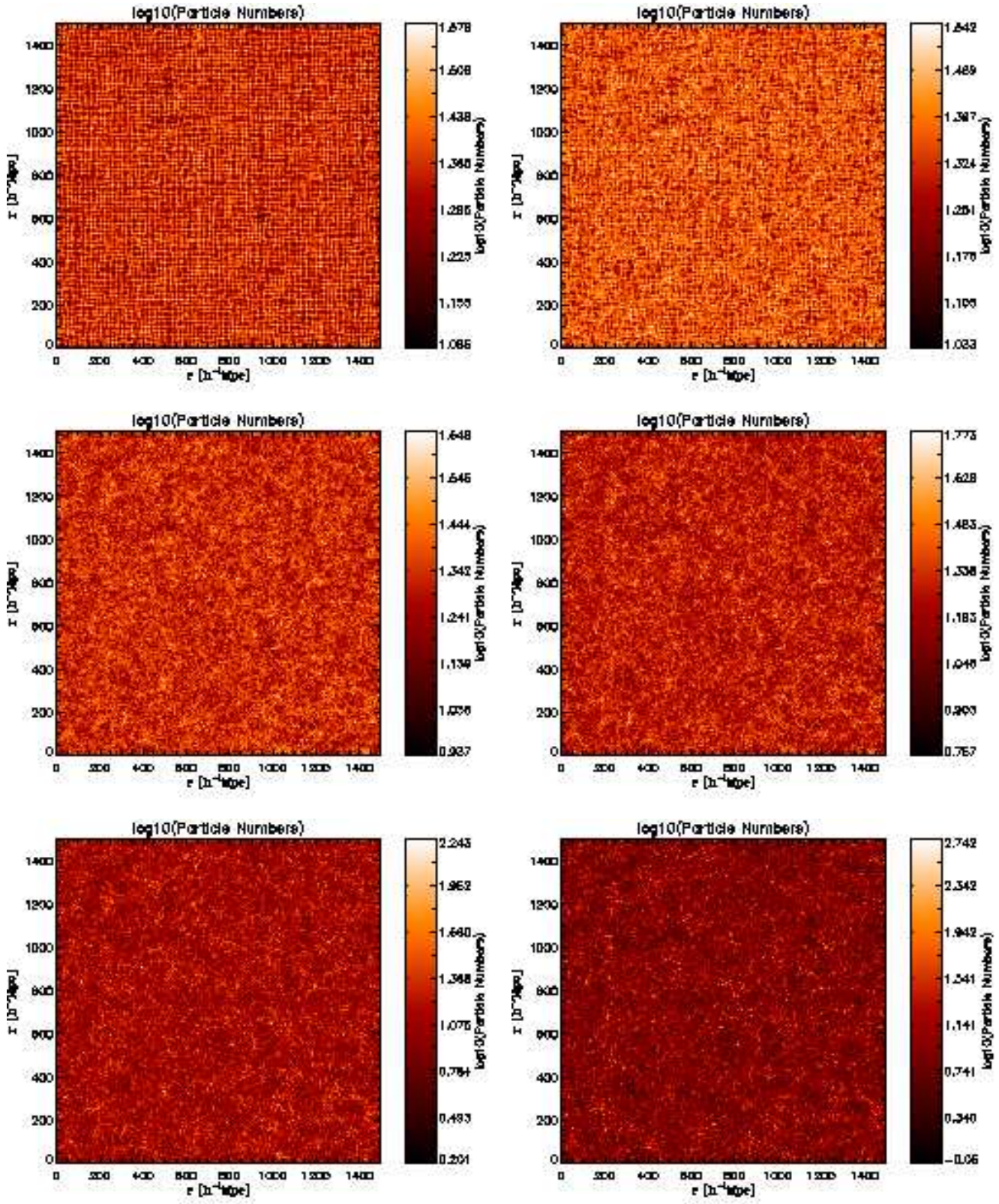

FIG. 1: Evolution of δ in a slab of thickness $\Delta x = 100\,h^{-1}$Mpc. The panels, going from left to right and top to bottom, represent redshifts: $z = \{15, 10, 5, 3, 1, 0\}$.

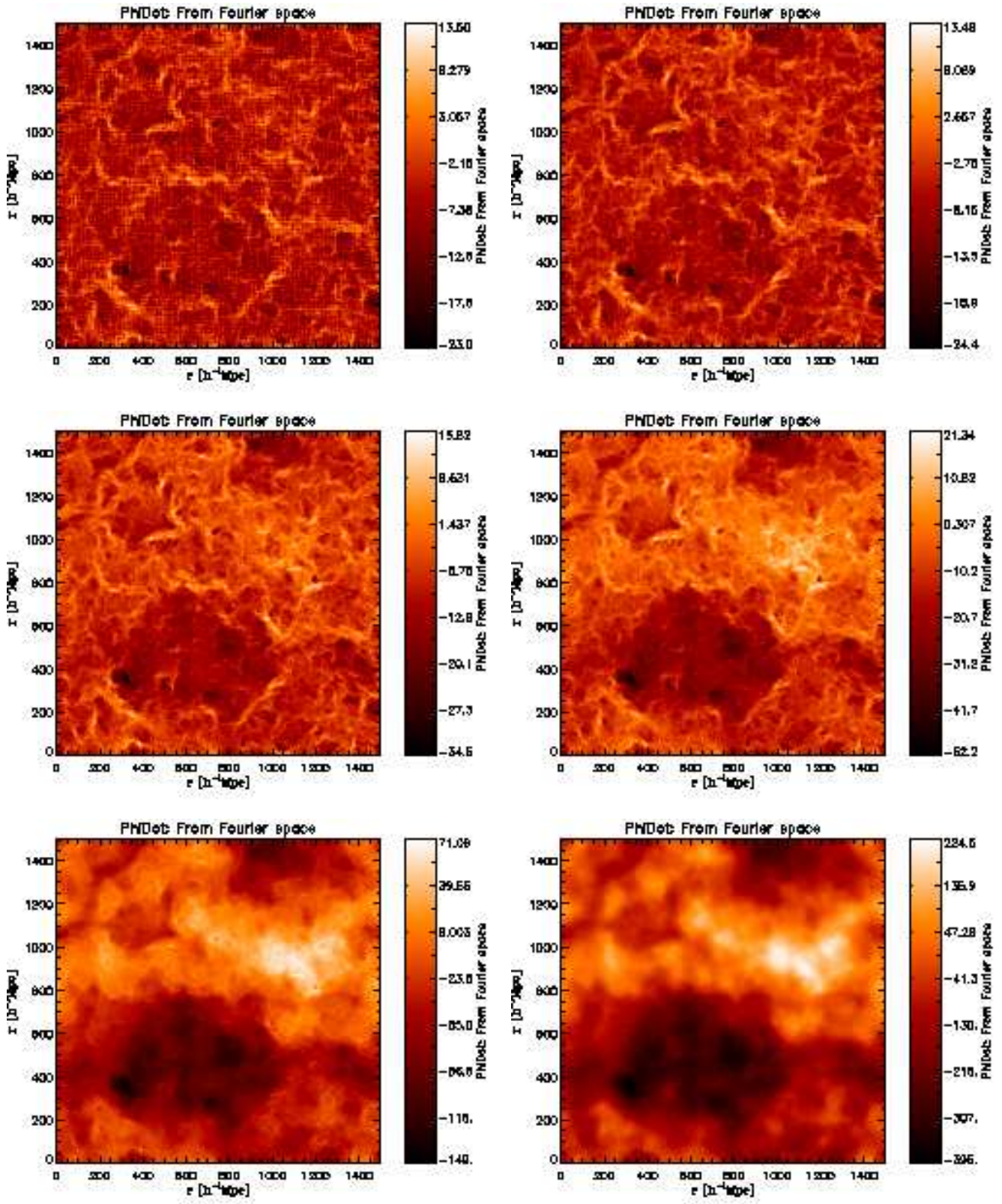

FIG. 2: Evolution of $\dot{\Phi}$ in a slab of thickness $\Delta x = 100\,h^{-1}$Mpc. The panels, going from left to right and top to bottom, represent redshifts: $z = \{15, 10, 5, 3, 1, 0\}$.

length $L = 1500\,h^{-1}$Mpc, evolves as a function of cosmic time from $z = 15$ to the present day. At early times, one can see that the Universe is regular and homogeneous, and the imprint of the initial grid configuration is still noticeable. At later times, gravitational instability of the matter has led to the formation of a pattern of web like structures with dense clumps at the vertices of the web – the 'Cosmic Web'. The point we wish to stress, is that it is difficult for the eye to pick out features that are larger than $100\,h^{-1}$Mpc.

Fig. 2 shows the evolution of $\dot{\Phi}(\mathbf{x}, t)$ as a function of cosmic time. At early times ($z \sim 15$), when there is no linear ISW, the maps are dominated by a small-scale foam-like structure. At later times, $z \sim 10$, the foam is sharpened and transformed, with butterfly like features present at the high density regions, as expected from the BG effect, i.e. a flow of mass moving transversely across the sky. At later times the dominating structures are on extremely large scales ($r > 500\,h^{-1}$Mpc), as expected by the linear late time ISW effect.

IV. DENSITY, MOMENTUM AND POTENTIAL POWER SPECTRA IN PT

A. The 3D power spectra

The perturbed fields of interest may be written as Fourier series,

$$\psi_\gamma(\mathbf{x}) = \sum_j \psi_\gamma(\mathbf{k}_j) \exp\left[-i\mathbf{k}_j \cdot \mathbf{x}\right] \ ; \tag{20}$$

$$\psi_\gamma(\mathbf{k}_j) = \frac{1}{V_\mu} \int d^3x \psi_\gamma(\mathbf{x}) \exp\left[i\mathbf{k}_j \cdot \mathbf{x}\right] \ , \tag{21}$$

where $\psi_\gamma \equiv \{\delta(\mathbf{x}), \nabla \cdot \mathbf{p}(\mathbf{x}), \dot{\Phi}(\mathbf{x})\}$, and where V_μ is some large region of the Universe over which we shall assume that the functions obey harmonic boundary conditions. Then, from translational invariance and isotropy, the correlation of different Fourier modes can be written

$$P_{\gamma_1\gamma_2}(k_i)\delta^K_{i,-j} \equiv V_\mu \left\langle \psi_{\gamma_1}(\mathbf{k}_i)\psi_{\gamma_2}(\mathbf{k}_j)\right\rangle \ , \tag{22}$$

where $P_{\gamma_1\gamma_2}$ is the power spectrum matrix of all of the fields. Using Eq. (9) we find, for example:

$$P_{\dot{\Phi}\dot{\Phi}}(k,a) = [\mathcal{F}(k)]^2 \left[\frac{H^2(a)}{a^2(t)} P_{\delta\delta}(k) - 2\frac{H(a)}{a^3(t)} P_{\omega\delta}(k) + \frac{1}{a^4(t)} P_{\omega\omega}(k)\right] \ ; \tag{23}$$

$$P_{\delta\dot{\Phi}}(k,a) = \mathcal{F}(k) \left[\frac{H(a)}{a(t)} P_{\delta_b\delta}(k) - \frac{1}{a^2(t)} P_{\delta_b\omega}(k)\right] \tag{24}$$

where we have defined $\omega(k;t) \equiv i\mathbf{k} \cdot \mathbf{p}(\mathbf{k};t) = \dot{\delta}(\mathbf{k};t)a(t)$.

B. Linear theory results

The two-point statistics may be evaluated easily within the linear theory: $\delta \ll 1$ and $\nabla \cdot \mathbf{v} \ll 1$. In this limit the Fourier mode of the density and its time derivative evolve as:

$$\delta(\mathbf{k};t) = D(t)\delta(\mathbf{k};t_0) \ ; \tag{25}$$

$$\dot{\delta}(\mathbf{k};t) = f(t)H(t)D(t)\delta(\mathbf{k};t_0) \ , \tag{26}$$

where we have the usual definition of the logarithmic derivative of the growth factor,

$$f(a) \equiv f(\Omega_m(a), \Omega_{\rm DE}(a)) \equiv \frac{\partial \log D(t)}{\partial \log a(t)} \ . \tag{27}$$

Hence we have

$$\begin{aligned} P^{\rm Lin}_{\omega\omega}(k,t) &= \left[a(t)\dot{D}(t)\right]^2 \left\langle |\delta(\mathbf{k};t_0)|^2 \right\rangle V_\mu \ ; \\ &= \left[a(t)f(a)H(t)D(t)\right]^2 P^{\rm Lin}_{\delta\delta}(k;t_0) \ ; \\ &= \left[a(t)f(a)H(t)\right]^2 P^{\rm Lin}_{\delta\delta}(k;t) \end{aligned} \tag{28}$$

and

$$\begin{aligned} P^{\rm Lin}_{\omega\delta}(k,t) &= a(t)\dot{D}(t)D(t) \left\langle |\delta(\mathbf{k};t_0)|^2 \right\rangle V_\mu \ ; \\ &= \left[a(t)f(a)H(t)\right] P^{\rm Lin}_{\delta\delta}(k;t) \ . \end{aligned} \tag{29}$$

Inserting these expressions into Eqs (23) and (24) gives:

$$P^{\rm Lin}_{\dot{\Phi}\dot{\Phi}}(k,t) = [\mathcal{F}(k)]^2 \left[\frac{H(a)}{a}\left(1 - f(a)\right)\right]^2 P^{\rm Lin}_{\delta\delta}(k;t) \tag{30}$$

$$P^{\rm Lin}_{\dot{\Phi}\delta}(k,t) = \mathcal{F}(k) \left[\frac{H(a)}{a}\left(1 - f(a)\right)\right] P^{\rm Lin}_{\delta\delta}(k;t) \ . \tag{31}$$

At this point we may note the well known result that, if the Universe is in an Einstein–de Sitter (EdS) phase of expansion (i.e. $\Omega_m(a) = 1$, and $D(a) \propto a$), then $f(a) = 1$ and the bracketed terms in Eqs (30) and (31) vanish, so the ISW effect vanishes. However, if the Universe is under/overdense in gravitationally active matter, then we expect a non-zero signal, which is positive for both spectra. In the currently favored LCDM model, $\Omega_{m0} \approx 0.25$, and so $1 - f(a) < 1$. However, at early times $\Omega_m \to 1$ and the ISW is shut off. In the next section we explore how this picture changes as the fields are evolved into the mildly nonlinear regime.

Before moving on though, we point out that in the literature there are a number of commonly used approximations for $f(a)$: for example, $f(a) \approx \Omega^{0.6}$ [36]; and somewhat better, $f(a) \approx \Omega_m(a)^{0.6} + \frac{\Omega_\Lambda(a)}{70}\left[1 + \frac{1}{2}\Omega_m(a)\right]$ [47] for models with a cosmological constant Λ; and better still the previous formula, but with the power-index of the first term $0.6 \to 4/7$ [48, 49]. However, all these approximations deviate at the few percent level when compared to the exact result obtained from numerically solving the differential equation for linear growth [for further details see for example 49, 50]. We therefore adopt the exact numerical solutions for both $D(a)$ and $f(a)$ throughout this study.

C. Beyond linear theory: Nonlinear PT

The collapse of cosmic structures can be followed into the nonlinear regime using standard perturbation theory (PT) methods, applied to an ideal fluid in a uniformly expanding spacetime [for an excellent review see 51]. The first application of PT methods to estimate the impact of the nonlinear evolution of $\dot{\Phi}$ on the CMB, was given by Seljak [15]. That work was conducted within the context of the flat SCDM model, and hence only provided an estimate for the Rees-Sciama contribution. Furthermore, owing to the fact that $(1-f)=0$ at all times in the EdS model, it was necessary only to calculate the PT up to 2nd order in δ, whereas in more general cosmologies, to be consistent at first order, one requires the corrections up to 3rd order. We shall now calculate the nonlinear ISW in the PT framework for the LCDM model.

To begin, we require from the PT theory the solutions for the fluid overdensity, and in Fourier space these may be written as,

$$\delta(\mathbf{k},t) = \sum_{n=1}^{\infty} [D(t)]^n \delta_n(\mathbf{k},t_0) \ , \tag{32}$$

where the perturbative solutions at each order can be written

$$\delta_n(\mathbf{k}) = \int \frac{\prod_{i=1}^{n}\left\{d^3q_i\,\delta_1(\mathbf{q}_i)\right\}}{(2\pi)^{3n-3}} \left[\delta^D(\mathbf{k})\right]_n F_n^{(s)}(\mathbf{q}_1,...,\mathbf{q}_n) \ . \tag{33}$$

In the above expression $\delta_1(\mathbf{q}_i)$ represents an initial field at wavenumber $\mathbf{q}_i$, and the nth order perturbed density depends on n initial fields. The quantities $F_n^{(s)}(\mathbf{q}_1,...,\mathbf{q}_n)$ represent the standard PT interaction kernels, symmetrized in all of their arguments. Also we have adopted the short-hand notation $\left[\delta^D(\mathbf{k})\right]_n = \delta^D(\mathbf{k}-\mathbf{q}_1-\cdots-\mathbf{q}_n)$. The Dirac delta function ensures that the waves conserve momenta through the interaction, i.e. $\mathbf{k}=\mathbf{q}_1+\cdots+\mathbf{q}_n$. For example, the second order PT kernel can be written,

$$F_2^{(s)}(\mathbf{q}_1,\mathbf{q}_2) \ = \ \frac{5}{7} + \frac{1}{2}\mu_{1,2}\left[\frac{q_1}{q_2}+\frac{q_2}{q_1}\right] + \frac{2}{7}\mu_{1,2}^2 \ , \tag{34}$$

where $\mu_{1,2} \equiv \hat{\mathbf{q}}_1 \cdot \hat{\mathbf{q}}_2$.

In the standard approach of nonlinear PT, the fluid equations are solved for the flat EdS background model. In this case the spatial and temporal parts of the evolution are fully separable and the perturbative solutions at each order simply scale as powers of the expansion factor $a(t)$ [52]. However, this is not the case for more general cosmological models, nevertheless a very good approximation to the evolution can be obtained by replacing the powers of $a(t) \to D(t)$. Strictly speaking, the PT interaction kernels also inherit some time dependence, however this is an extremely weak function of time and so to a very good approximation we may use the kernels from the flat EdS case [for deeper discussion of this see 51].

As Seljak [15] showed, to calculate the ISW we simply require the PT expansion for δ and its time derivative. Using Eq. (32), this latter quantity may be written,

$$\dot{\delta}(\mathbf{k},t) = f(a)H(a)\sum_{n=1}^{\infty} n[D(t)]^n \delta_n(\mathbf{k},t_0) \ . \tag{35}$$

These quantities may now be used to compute the Next-to-Leading-Order (NLO) corrections to the power spectra. Using the above expressions plus the standard PT techniques we find, for pseudo-momentum:

$$P_{\omega\omega}^{\rm NL} \ = \ P_{\omega\omega}^{\rm Lin} + P_{\omega\omega}^{\rm 1Loop} \ ; \tag{36}$$
$$P_{\delta\omega}^{\rm NL} \ = \ P_{\omega\delta}^{\rm Lin} + P_{\omega\delta}^{\rm 1Loop} \ ; \tag{37}$$

where the one-loop corrections are,

$$P_{\omega\omega}^{\rm 1Loop} \ = \ [af(a)H(a)]^2\left[4P_{\delta\delta}^{22}(k,a)+3P_{\delta\delta}^{13}(k,a)\right] \tag{38}$$
$$P_{\delta\omega}^{\rm 1Loop} \ = \ [af(a)H(a)]\,2P_{\delta\delta}^{\rm 1Loop}(k,a) \ . \tag{39}$$

For the $\dot{\Phi}$ we find:

$$P_{\dot{\Phi}\dot{\Phi}}^{\rm NL} \ = \ P_{\dot{\Phi}\dot{\Phi}}^{\rm Lin} + P_{\dot{\Phi}\dot{\Phi}}^{\rm 1Loop}; \tag{40}$$
$$P_{\delta\dot{\Phi}}^{\rm NL} \ = \ P_{\delta\dot{\Phi}}^{\rm Lin} + P_{\delta\dot{\Phi}}^{\rm 1Loop}, \tag{41}$$

where the one-loop corrections are,

$$P_{\dot{\Phi}\dot{\Phi}}^{\rm 1Loop}(k) \ = \ [\mathcal{F}(k)]^2\frac{H^2(a)}{a^2}\Big\{\,[1-2f(a)]^2P_{\delta\delta}^{22}(k) + [1-3f(a)][1-f(a)]P_{\delta\delta}^{13}(k)\Big\} \ ; \tag{42}$$

$$P_{\delta\dot{\Phi}}^{\rm 1Loop}(k) \ = \ \mathcal{F}(k)\frac{H(a)}{a}\Big\{\,1-2f(a)\Big\}\,P_{\delta\delta}^{\rm 1Loop}(k,a) \tag{43}$$

In the above expression $P_{\delta\delta}^{22}$ and $P_{\delta\delta}^{13}$ are the NLO corrections to the matter power spectrum and we defined, $P_{\delta\delta}^{\rm 1Loop}(k,a) \equiv P_{\delta\delta}^{13}(k,a) + P_{\delta\delta}^{22}(k,a)$ [for explicit forms for the 1Loop expressions, see 52–54].

We may now learn how the NLO corrections entangle the pure linear ISW decay of potentials with the nonlinear RS effects. The easiest way to discern the changes is to consider the sign of the corrections in the above equations. We notice that there are two ways the sign may change: firstly, there is a sign flip with scale, since $P_{\delta\delta}^{13}$ is negative and dominant on large scales and $P_{\delta\delta}^{22}$ is positive and dominant on smaller scales; secondly, the time dependent prefactors may change sign.

Considering the time dependent factors, we see that the cross-power spectrum, Eq.(43), will only change sign when, $1-2f(a)=0$, which occurs when $\Omega \approx 0.3$. We shall label this time $a_{\rm RS}$. Table I summarizes the changes.

TABLE I: Sign of the NLO correction to the $P_{\delta\dot{\Phi}}(k)$ power spectrum. Recall that a positive correction means an increase in the decay rate of the potentials. See text for further details.

Sign of correction	$\lvert P_{13}(k)\rvert > P_{22}(k)$	$\lvert P_{13}(k)\rvert < P_{22}(k)$
$\Omega_m > \Omega_m(a_{\rm RS})$	$(+)$	$(-)$
$\Omega_m < \Omega_m(a_{\rm RS})$	$(-)$	$(+)$

The key point to notice is that at early times, there is an enhancement of the ISW on very large scales (i.e. enhanced decay of gravitational potentials) and on small scales there is a suppression of ISW effect (growth of potentials). Then, at late times $z < z_{\rm RS}$ these corrections invert themselves and ISW is suppressed on large scales and small-scale potentials decay.

Turning now attention to the auto-power correction, Eq. (42), we see that the prefactor multiplying $P^{22}_{\delta\delta}$ is always positive, whereas the second term only switches sign when $1 - f < 0$ or $1 - 3f > 0$. However since $\Omega_m < 1$, the first bracket will never switch sign and will vanish at early times. On the other hand the second bracket remains negative until $\Omega_m \approx 0.16$. Given current constraints on $\Omega_{m0} \sim 0.25$ the second bracketed term is always negative and on multiplying by $P^{13}_{\delta\delta}$, we conclude that it too is always positive.

D. Evolution of density power spectrum

Fig. 3 shows the evolution of the nonlinear matter power spectrum measured from $z = 1$ to the present day. The power is plotted from the fundamental mode, $k = 2\pi/L \approx 0.005\,h\,{\rm Mpc}^{-1}$ to half of the Nyquist frequency of the mesh $k_{\rm NY} = \pi N_{\rm g}/L \approx 2\,h\,{\rm Mpc}^{-1}$, where we use $N_{\rm g} = 1024$ for all transforms. Above this frequency the power in the Fourier modes is affected by aliasing from smaller scales [55]. In the top panel we show the mean ensemble averaged absolute power from the simulations at each epoch, colored points with errors. On the largest scales $k < 0.1$, the power grows by a factor of ~ 2 from $z = 1$ to 0, and there appears to be very good agreement with the linear theory predictions on these scales (colored solid lines). On smaller scales the power is significantly amplified.

In the bottom panel of the Fig. 3 we take the ratio of the data with the linear theory, and to see clearly the effects for each snapshot, we offset the curves by 0.1 in the vertical direction, with the solid colored lines being the baseline for each corresponding snapshot. We see that there is a small ($\approx 2 - 3\%$) suppression of power at late times for modes $0.05 < k < 0.1\,[\,h\,{\rm Mpc}^{-1}]$, this is termed the 'previrialization feature' [54, 56, 57]. On smaller scales ($k > 0.1\,h\,{\rm Mpc}^{-1}$) the power is strongly amplified, compared to linear theory. In this panel we also present the predictions from the standard PT (described in §IV C) and we see that it qualitatively captures the trends in the data. However, in closer detail, we see that the PT over estimates the power on smaller scales and that the predictions become progressively worse at higher expansion factors and higher wavenumbers.

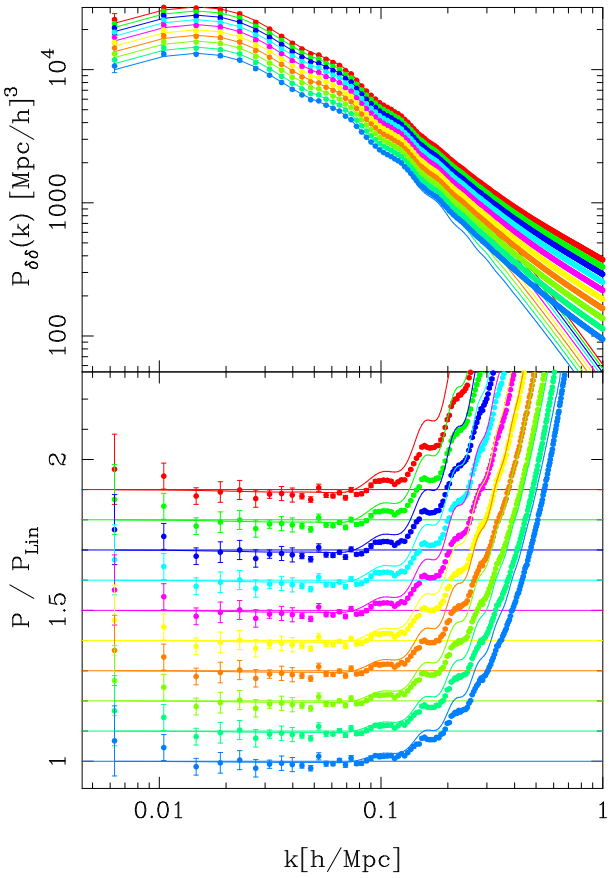

FIG. 3: The time evolution of the nonlinear CDM density power spectrum as a function of wavenumber. *Top panel*: colored points denote the absolute power and error bars are on the mean and are determined from the ensemble of simulations. The thin lines denote the linear theory and from top to bottom results are for expansion factors: $a = \{1.0, 0.93, 0.87, 0.76, 0.66, 0.62, 0.57, 0.54\}$. *Bottom panel*: the ratio of the power spectra with respect to the linear theory prediction. The thick solid lines denote the predictions from the nonlinear Eulerian PT. Note that for clarity the measurements have been offset by 0.1 in the vertical direction.

E. Evolution of the pseudo-momentum spectra

In Figs 4 and 5 we present the pseudo-momentum–density cross- and pseudo-momentum auto-spectra, respectively. Again the top part of each figure shows the absolute power and the bottom the ratio with respect to the linear model (c.f. Eqs 28 and 29). Note that the spectra are amplified relative to the density spectrum, and that on large scales this boost is well captured by multiplicative powers of $af(a)H(a)$. In addition, we find that on very large scales, the momentum spectra also display a previrialization feature and that the suppression of power appears to be deeper in both cases. Furthermore, on smaller scales the nonlinear amplification, which occurred at around $k \sim 0.1\,h\,{\rm Mpc}^{-1}$ for $P_{\delta\delta}$, appears at larger scales in both cases, with the $P_{\omega\omega}$, strongly amplified by $k > 0.7\,h\,{\rm Mpc}^{-1}$. We compare these measurements with the predictions from standard PT and find for $P_{\delta\omega}$ reasonably good agreement on very large scales and an over prediction on smaller scales. However, for $P_{\omega\omega}$ the agreement is much better.

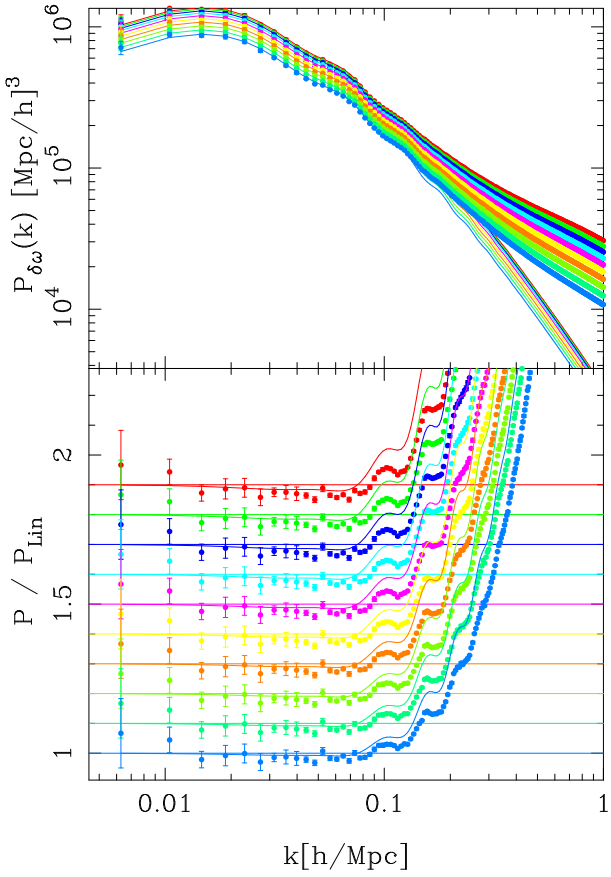

FIG. 4: The evolution of the pseudo-momentum–mass density cross-power spectra from $z = 1$ to 0, as a function of spatial wavenumber. Points and lines are as for Fig. 3.

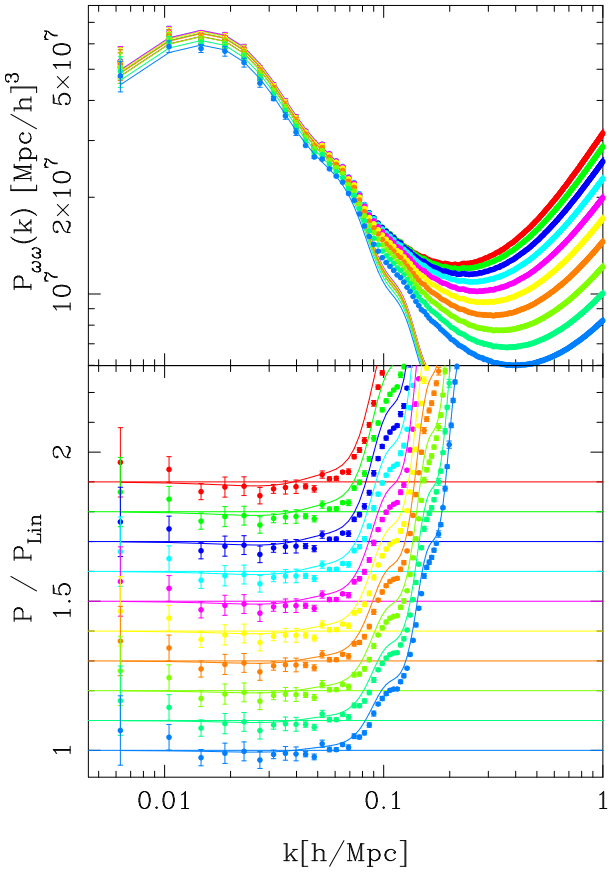

FIG. 5: The evolution of the pseudo-momentum auto-power spectra from $z = 1$ to 0, as a function of spatial wavenumber. Points and lines are as for Fig. 3.

F. Evolution of the $\dot{\Phi}$ power spectra

Having examined the individual components of the $P_{\dot{\Phi}\dot{\Phi}}$ spectrum we may now sum them together with weights as given by Eq. (23). Following Seljak [15] and Cai et al. [17], we introduce the dimensionless and rescaled form of $P_{\dot{\Phi}\dot{\Phi}}$,

$$\Delta^2_{\dot{\Phi}\dot{\Phi}}(k) \equiv \frac{4\pi}{(2\pi)^3}\frac{k^3 P_{\dot{\Phi}\dot{\Phi}}(k)}{[\mathcal{F}(k)H(a)/a]^2}\ ; \tag{44}$$

$$= \frac{k^3}{2\pi^2}\left[P_{\delta\delta}(k) - \frac{2P_{\omega\delta}(k)}{H(a)a(t)} + \frac{P_{\omega\omega}(k)}{H^2(a)a^2(t)}\right] \tag{45}$$

Fig. 6 shows the evolution of the ensemble averaged $\Delta^2_{\dot{\Phi}\dot{\Phi}}$, with errors on the mean. The top panel shows the absolute spectra for the 10 snapshots from $z = 1$ to the present day. Also shown as the thin solid lines are the predictions from the linear theory as given by Eq. (30). Again, there appears to be good agreement on large scales, and nonlinear amplification on smaller scales. The bottom panel presents the ratio with respect to the linear model, again we have offset different epochs by 0.1 in the vertical direction for clarity. There is clear evidence for nonlinear amplification of the spectrum on the very largest scales, and relative to linear theory this becomes increasingly more important at higher redshifts, as expected. Indeed by $k = 0.03\,h\,\mathrm{Mpc}^{-1}$ and at $z \sim 1.0$ the power is more than 10% in excess of the linear theory prediction, whereas at $z = 0$, a 10% amplification is only achieved by $k \sim 0.07\,h\,\mathrm{Mpc}^{-1}$. Here we also show the predictions from the NLO PT calculation from Eqs (40) and (42), and we note a startlingly good agreement at all epochs.

That the nonlinear effects become increasingly important at higher redshifts follows directly from the fact that $1-f(a) \to 0$ as $a \ll 1$. In this case, the only contribution to the spectrum comes from the nonlinear Rees-Sciama effect, and in the limit $a \to 0$ it is given by

$$\Delta^2_{\dot{\Phi}\dot{\Phi}}(k) \to \frac{k^3}{2\pi^2}[1-2f(a)]^2 P^{22}_{\delta\delta}(k)\ . \tag{46}$$

On comparing our results with Fig. 1 from Cai et al. [17], we find qualitatively good agreement. However, on the largest scales their spectra do not appear to reproduce the linear theory at high precision. The excess signal that they find compared to the linear theory, we believe, is a result of using the approximation $f \approx \Omega_m^{0.6}$. Some of the discrepancy may also be due to cosmic vari-

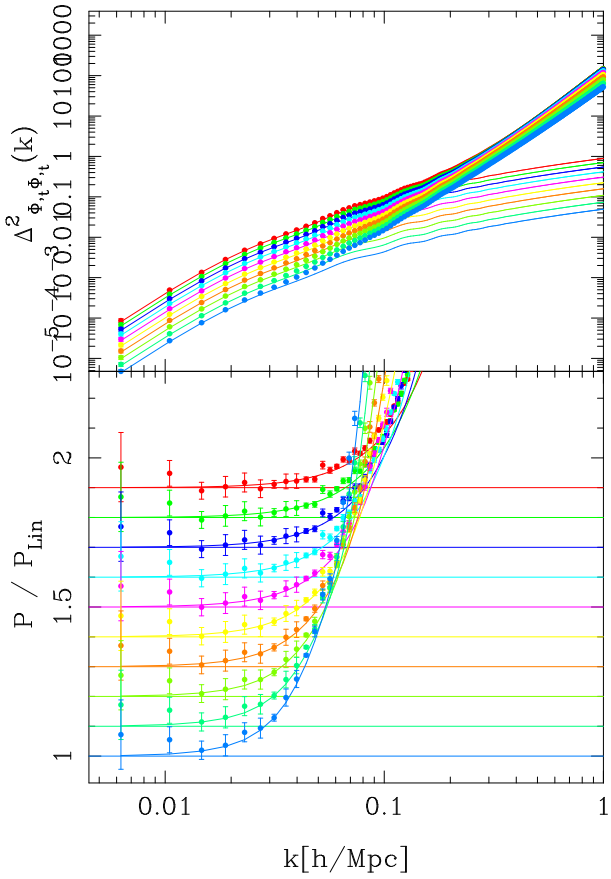

FIG. 6: Evolution of the $\dot\Phi$ auto-power spectra from $z = 1$ to 0 in dimensionless units, as a function of spatial wavenumber. Again points and lines are as presented in Fig. 3.

ance, since they only show results for a single simulation. In that work the authors also proposed a nonlinear correction formula for $P_{\dot\Phi\dot\Phi}$, which has two free parameters. Since the PT has no free parameters, and as it provides an excellent match to the data for the scales $k < 0.1$ we consider our approach a sufficient description on these large scales. Such fitting would most likely be necessary on smaller scales for good agreement, but these scales are of diminishing importance for the calculation of the CMB C_l spectrum for $l < 100$.

V. RESULTS: IMPACT ON CMB SPECTRUM

The CMB temperature fluctuations arising from the ISW may be decomposed using a spherical harmonic expansion, and the amplitude of each harmonic can be written as [11, 29],

$$a^{\rm T}_{lm} = (-i)^l 4\pi \int \frac{d^3k}{(2\pi)^3} Y^*_{l,m}(\hat{\mathbf{k}}) \Delta^{\rm T}_l(k, a_{ls}) \ , \qquad (47)$$

with,

$$\Delta^{\rm T}_l(k) \equiv \int_0^{\chi_{\rm max}} d\chi \frac{2a}{c^3} j_l(k\chi) \dot\Phi(k, \chi(t)) \ , \qquad (48)$$

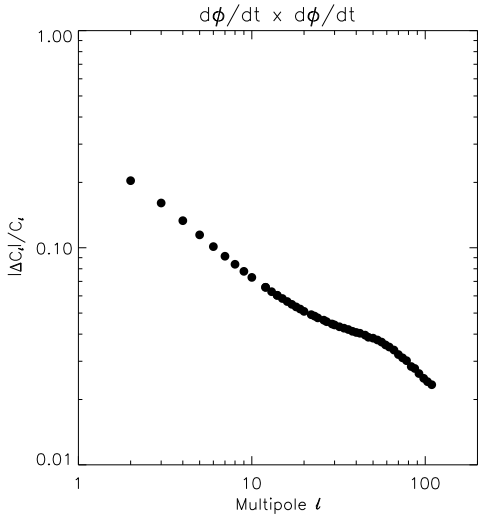

FIG. 7: Relative error ($[C_l^{\rm Limber} - C_l^{\rm Exact}]/C_l^{\rm Exact}$) between the Limber approximation and the exact C_l computation of the CMB angular power spectrum. Results are shown for $k = (l + 1/2)/D_A$ replacement.

where we transformed Eq. (1) to comoving geodesic distance χ and $\chi_{\rm max}$ is the distance from the observer to the surface at which the ISW first becomes significant. The power in the harmonic multipoles may be calculated using the standard methods, and the ISW temperature spectrum may be written:

$$C_l^{TT} = \frac{2}{\pi} \int dk k^2 \int_0^{\chi_{\rm max}} d\chi_1 d\chi_2 j_l(k\chi_1) j_l(k\chi_2) \times \frac{4 a_1 a_2}{c^6} P_{\dot\Phi\dot\Phi}(k; \chi_1, \chi_2) \ . \qquad (49)$$

In the limit ($l > 10$) we may use the Limber approximation to simplify the above integrals [see for example 12, 15, 58]. Assuming that only modes transverse to the line of sight contribute to the signal and also that the power spectra are slowly varying functions of k, then the orthogonality of the spherical Bessel functions gives,

$$\int dk k^2 j_l(k\chi_1) j_l(k\chi_2) \mathcal{P}_\alpha(k, \chi_1, \chi_2) \approx \frac{\pi}{2} \frac{\delta^D(\chi_1 - \chi_2)}{\chi_1^2} \mathcal{P}_\alpha\left(\frac{l}{D_A(\chi_1)}\right) \ . \qquad (50)$$

where $D_A(a)$ is the comoving angular diameter distance ($D_A(a) = \chi(a)$ for flat space). On applying this approximation the above expression reduces to the simple form:

$$C_l^{TT} \approx \int_0^{\chi_{\rm max}} d\chi \frac{4a^2}{c^6} P_{\dot\Phi\dot\Phi}\left(k = \frac{l}{D_A(\chi)}, \chi\right) \frac{1}{\chi^2} \ ; \qquad (51)$$

$$\approx \frac{4}{c^5} \int_{a_{\chi({\rm max})}}^{a_0} da \, P_{\dot\Phi\dot\Phi}\left(k = \frac{l}{D_A}, a\right) \frac{1}{H(a)\chi^2} \qquad (52)$$

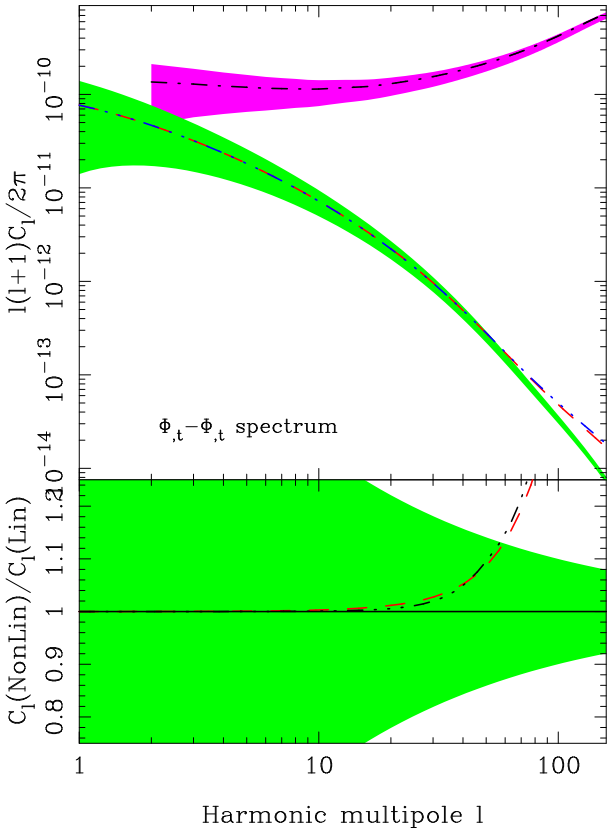

FIG. 8: *Top panel*: Angular power spectrum of CMB temperature fluctuations as a function of harmonic multipole. ISW contributions: solid green shaded region – linear theory with encompassing 1-σ Gaussian error domain; red dash line – nonlinear PT; ensemble average N-body measurement – blue triple dot dash curve. The CMB primary anisotropy spectrum is given by the magenta dot-dash curve and its 1-σ Gaussian error domain by the solid magenta shaded region. *Bottom panel*: ratio of the nonlinear ISW spectra to the linear theory spectrum. While this can exceed the 1-sigma error of ISW alone (as shown), it is always less than the 1-sigma error band of the overall CMB (not shown), hence the nonlinear effects are not detectable in the CMB power spectrum.

Fig. 7 compares the Limber approximate expressions for the angular power spectrum of temperature fluctuations with the exact spherical harmonic line-of-sight integration. On scales $l < 10$, the Limber approximation is clearly poor with relative errors being $> 10\%$. The transformation $k = (l + 1/2)/D_A$, as suggested by Ho et al. [27], Loverde and Afshordi [59], improves the approximation, but the errors still remain large. However for $l > 10$, the error is reduced and by $l = 20$ it is of the order $\sim 5\%$ (for a detailed discussion on the validity of the Limber approximation for different power spectra, see Appendix A). We shall nevertheless adopt the Limber approximation for our theoretical analysis, but note that if significant effects are apparent on multipoles $l < 30$, then only a full spherical harmonic analysis will give robust results. However, this would necessarily involve computing the unequal time correlations of the Fourier modes of $\dot{\Phi}(\mathbf{k}, t)$.

Fig. 8 shows the results for the Limber approximated ISW temperature angular auto-power spectrum. We scale the C_l spectrum by $l(l + 1)$ in the usual way and restrict our attention to angular modes $l < 100$. In the upper panel of the figure we compare three predictions: the linear theory calculation with 1-σ cosmic variance errors, denoted by the green shaded region; the nonlinear PT, denoted by the red dash line; and the mean measurement from the N-body simulations blue triple dot-dash curve. The 1-σ green shaded error region was computed using the Gaussian variance formula:

$$\frac{\Delta C_l^{TT}}{C_l^{TT}} = \sqrt{\frac{1}{f_{\rm sky}}\frac{2}{2l+1}}\,, \tag{53}$$

where $f_{\rm sky}$ is the fraction of sky covered, and we shall take this to be of order unity. The estimate of the C_l spectrum from the N-body simulations was obtained by the following prescription: we first made an array of the measured $\mathcal{P}_{\dot{\Phi}\dot{\Phi}}(k)$ spectra and divided this through by the linear theory ISW power spectrum at that epoch. On very large scales the ratios all asymptotically approach unity and so the only evolution that remains to be modeled is the higher k domain. To do this, we employ the bi-cubic spline routine [55] and interpolate the spectra in $\log_{10}[a]$ and $\log_{10}[k]$. Note that on scales greater than the fundamental mode of the simulation cube the bi-cubic spline gives unity and we recover exactly linear theory. We emphasize the importance of this step, since otherwise the C_l^{TT} spectra will be significantly reduced for $l < 10$, owing to the finite volume of the simulations. Note that in order to avoid extrapolating the bicubic spline fits into regions where we have no measured data, the upper redshift limit of the Limber integrals was set to $z = 1$. We have tested that this does not change our results in any significant way, by computing the PT out to $z = 5$.

In Fig. 8, we see that all three theoretical predictions converge for $l < 30$, however for $l > 30$ we find enhancement of the signal for both the PT and N-body results and that these agree to high precision, in agreement with expectations from Fig. 6. By $l = 50$ they both show between $\sim 10-15\%$ increase in the power. We also show the CMB primary anisotropy power spectrum as the black dot-dash line, with the magenta shaded band giving the cosmic variance errors, Eq. (53). The primary C_l spectrum was obtained using the `cmbfast` routine with cosmological parameters to match those of the `zHORIZON` simulations. Note that, by default, this spectrum already includes the linear ISW effect.

Comparing the primary with the ISW signal, we see that at $l = 30$ the primary signal is two orders of magnitude larger, and so the nonlinear enhancement at these multipoles will induce changes to the CMB spectrum that are $\ll\sim 1\%$. While the nonlinear effect exceeds cosmic variance in ISW for $l > 50$, it never exceeds the cosmic variance from the total CMB, since ISW contribution

to CMB decreases with l. Our findings are consistent with earlier results [12, 17], but are established with improved precision. We therefore do not expect large-scale nonlinear evolution of the gravitational potentials to be responsible for any anomalies in WMAP angular power spectrum.

VI. ISW-DARK MATTER CROSS-CORRELATION SPECTRUM

Having discussed the ISW auto-correlation spectrum we now move on to discussing ISW correlation with the density field. We begin with the dark matter density $C_l^{T\delta}$. This can be observed by cross-correlating the CMB with the weak lensing signal of galaxies [60, 61], the weak lensing of 21cm transitions [62] or the weak lensing of CMB itself (with information encoded in CMB bispectrum) [33, 63]. In addition, there are a number of advantages to be gained from studying this: firstly, there exists an "alternative" method for estimating $P_{\dot\Phi\delta}$, and this provides us with an independent check on our "standard method", described in §II; secondly, owing to the larger number of dark matter particles, the effects of shot noise on the spectra can be better assessed, and as we will show for the alternate method, more easily corrected for.

A. Alternative estimator for $P_{\dot\Phi\delta}$

Our alternative approach to estimating $P_{\dot\Phi\delta}$ can be understood as follows: Consider the ensemble average of the product of $\delta(k)$ and $\dot\Phi(k)$, using Poisson's equation we may rewrite this as,

$$\begin{aligned} P_{\delta\dot\Phi}(\mathbf{k},a) &= V_\mu \left\langle \delta(\mathbf{k},a)\dot\Phi^*(\mathbf{k},a)\right\rangle \ , \\ &= -a[\mathcal{F}(k)]^{-1}V_\mu \left\langle \Phi(\mathbf{k},t)\dot\Phi^*(\mathbf{k},a)\right\rangle \ , \\ &= -a[\mathcal{F}(k)]^{-1}P_{\dot\Phi\Phi}(\mathbf{k},a) \ . \end{aligned} \tag{54}$$

We now take advantage of the useful property that

$$P_{\Phi\dot\Phi}(\mathbf{k},a) = \frac{1}{2}\frac{\partial}{\partial t}P_{\Phi\Phi}(\mathbf{k},a) = \frac{1}{2}aH(a)\frac{\partial}{\partial a}P_{\Phi\Phi}(\mathbf{k},a) \ . \tag{55}$$

Through further use of Poisson's equation, the last term in the above equation may be rewritten in terms of the density power spectrum, i.e. $P_{\Phi\Phi}(\mathbf{k},t) = \left[\mathcal{F}(k)/a\right]^2 P_{\delta\delta}(\mathbf{k},a)$. Putting this together, we arrive at the result [33],

$$\begin{aligned} P_{\dot\Phi\delta}(\mathbf{k},a) &= -\frac{1}{2}a^2H(a)\mathcal{F}(k)\frac{\partial}{\partial a}\left[\frac{P_{\delta\delta}(\mathbf{k},a)}{a^2}\right] \ , \\ &= -\frac{1}{2}aH(a)y(k,a)\mathcal{F}(k)\frac{\partial \ln y}{\partial \ln a} \ , \end{aligned} \tag{56}$$

where $y \equiv \left[P_{\delta\delta}(\mathbf{k},a)/a^2\right]$. This simple expression informs us that the ISW cross-correlation can also be estimated from just two things: the matter power spectrum and its evolution with time. We may check that the above expression is consistent with our previous result (c.f. Eq. 24). On assuming linear theory $P_{\delta\delta}(\mathbf{k},a) = D^2(a)P_{\rm Lin}(k)$, then we find

$$\frac{\partial \ln y}{\partial \ln a} = 2\left[f(a) - 1\right] \ , \tag{57}$$

and on insertion of the above expression into Eq. (56), we recover our earlier result.

The practical implementation of the above algorithm requires us to estimate the time derivative of the power spectrum, and we do this using the usual time-centered difference scheme:

$$\frac{\partial \ln y}{\partial \log a} \approx \frac{1}{y_i}\frac{y_{i+1} + y_{i-1}}{\left[\log a_{i+1} - \log a_{i-1}\right]} \ , \tag{58}$$

where $y_i \equiv y(a_i)$ is the estimate at epoch a_i. Note that since we employ a time-centered difference scheme, we do not show results for for $z = 0$ or $z = 1$, the first and last epochs considered.

B. Results: evolution of $P_{\dot\Phi\delta}$

Fig. 9 compares the results for $P_{\dot\Phi\delta}$ obtained from our standard method (c.f. Eq.24) of solving the continuity equation (black points with errors), with our alternative method (colored points with errors). As was done for $P_{\dot\Phi\dot\Phi}$ we have introduced a dimensionless and scaled form of the cross-power spectrum (c.f. Eq. 45):

$$\Delta^2_{\delta\dot\Phi}(k) \equiv \frac{4\pi}{(2\pi)^3}\frac{k^3P_{\delta\dot\Phi}(k)}{\left[\mathcal{F}(k)H(a)/a\right]} \ ; \tag{59}$$

$$= \frac{k^3}{2\pi^2}\left[P_{\delta\delta}(k) - \frac{P_{\delta\omega}(k)}{H(a)a(t)}\right] \ . \tag{60}$$

The left panel of Fig. 9 shows that the two independent approaches produce results that agree to high precision. We are therefore confident that both methods are consistent and implemented correctly.

The top panel compares the spectra estimated from the simulations (points with error bars) and the linear theory predictions (solid lines). The lower panels show the ratio with respect to the linear predictions. There are a number of important features that we draw attention to: firstly, rather than nonlinear effects becoming increasingly prominent with time, we see that they are stronger at earlier times and on larger scales. The explanation follows our earlier discussion of Fig. 6, and owes to the fact that the linear ISW effect switches off as $a \to 0$ and $1 - f(a) \to 0$, leaving only the RS contributions (c.f. §IV C).

Next, we note that there is a sign change in the spectra as one goes from low to high k. Since we plot the absolute value of the power the sign change is understood to be the point where the signal drops to zero and bounces back up. The scale at which this sign change occurs is a function of time, and it appears on larger scales at higher

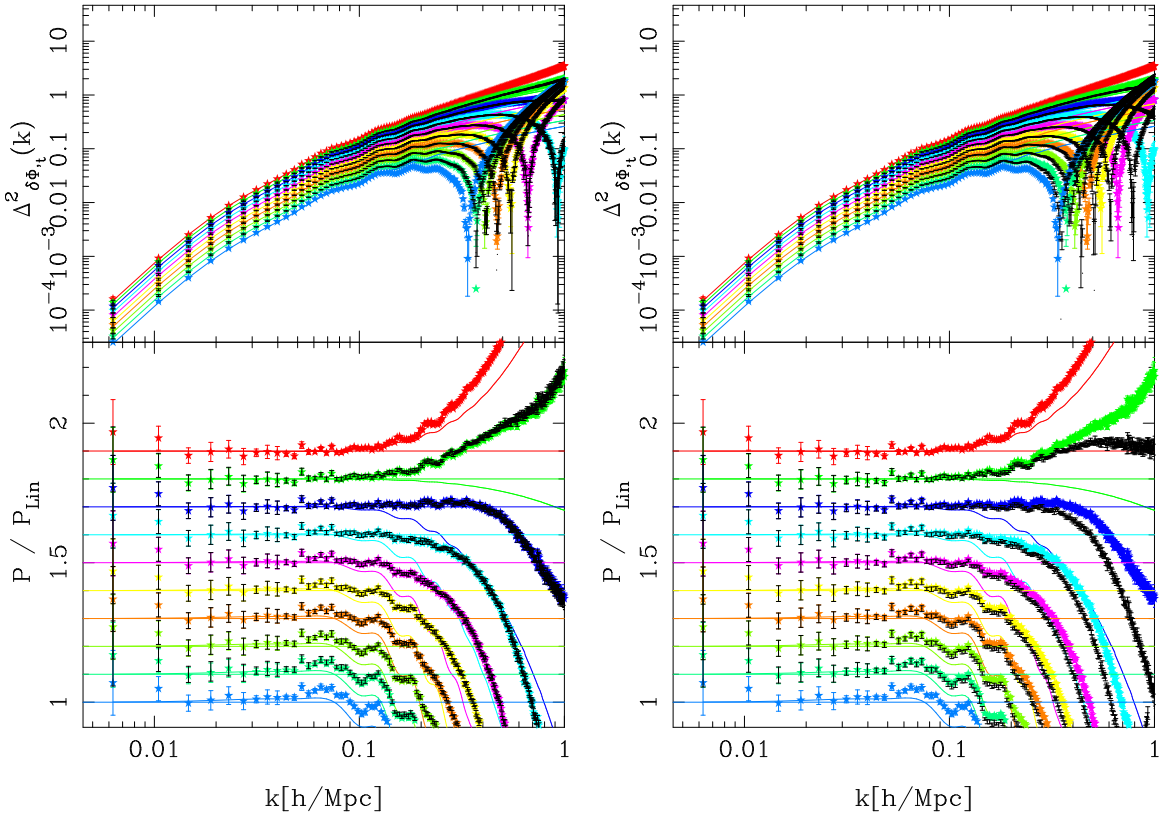

FIG. 9: Comparison of $P_{\dot{\Phi}\delta}$ estimates obtained from standard method (continuity equation) and the alternate method (time derivative of $P_{\delta\delta}$, c.f. Eq. 56). Colored points with errors denote the standard method, and black points with errors denote the alternate method. *Left panel*: no shot noise correction. *Right panel*: shot noise correction applied to the alternative method. Top sections show absolute power, lower sections show the ratio with respect to the linear theory, and for clarity the results at each epoch have been offset from each other by 0.1 in the vertical direction. The lines in the bottom panels denote the predicitons form the standard PT and from top to bottom results are for expansion factors: $a = \{1.0, 0.93, 0.87, 0.76, 0.66, 0.62, 0.57, 0.54\}$.

redshifts [see also 17]. The sign change is due to the fact that the $\dot{\Phi}$ signal becomes dominated by the RS and BG effects. However, for the spectra with $z < 0.3$ we see no sign change over the k-range that we consider. Moreover, unlike the lower redshift epochs we see an amplification relative to the linear theory. This means that, at late times in LCDM model, nonlinear evolution can actually *enhance* the decay of gravitational potentials, consistent with our earlier discussion of the PT (c.f. §IV C). Further support for the PT interpretation of this phenomenon comes from the fact that if one considers the results at high redshift, then around $k \sim 0.1\,h\,\mathrm{Mpc}^{-1}$ there is a small amplification of power with respect to the linear model.

In the discussion so far we have neglected the issue of the discreteness correction due to finite number of dark matter particles. It is unclear how to apply the shot noise correction to the momentum density. However, since we know the shot noise correction on the dark matter power spectrum is $P_{\delta\delta} \to P_{\delta\delta} - 1/\bar{n}$, where $\bar{n}$ is the number density of dark matter particles, the discreteness effects may be accounted for more easily when using Eq. (56). Fig. 9, right panel, shows the results obtained from this procedure. Whilst we see that the correction reduces the spectra by a small amount for all $k > 0.2$, we nevertheless see that both the small-scale late-time amplification and early-time large-scale amplification of the $P_{\dot{\Phi}\delta}$ remain significant. We are therefore led to conclude that, nonlinear evolution *may* lead to a small enhancement of the ISW in the LCDM model.

Comparing our results with the measurements of $P_{\delta\dot{\Phi}}$ from Cai et al. [17], we observe that these authors find no such late time amplification. Owing to the fact that we have provided two independent methods to obtain the estimates, and since we have a significantly larger total simulation volume ($\sim$ 12 times larger) furnishing smaller errors, we believe that our result is robust. In the next section we shall investigate whether selecting highly biased regions may influence these results further.

VII. ISW-HALO CROSS-CORRELATION SPECTRUM

The cross-correlation between $\dot{\Phi}$ and a density tracer field is more easily observable than with the density field

itself, which so far is limited because of the small area or large errors in the weak lensing reconstruction. One consequence of this is the added complication of needing to understand the bias relation – the mapping from the tracer population to the underlying dark matter density. In this Section we shall explore whether the cross-correlation of $\dot{\Phi}$ with cluster- and group-scale dark matter haloes, measured in the `zHORIZON` simulations, between $z = [0.0, 1.0]$, changes the ISW signal in any significant way, beyond a linear bias. From the assumption that all galaxies reside in dark matter haloes, it follows that the large scale clustering properties of any galaxy sample are a weighted average of the halo clustering statistics. Consequently, studying the halo-ISW cross-correlations should provide representative results for a number of plausible surveys. In particular, while we are limited by the mass resolution of our simulations so that our analysis only applies to biased halos with bias $b > 2$, we note that most of the data sets used for ISW detection so far are based on strongly biased tracers Giannantonio et al. [26], Ho et al. [27], so our results are applicable to these.

A. Linear Theory

In nearly all ISW studies to date the bias has been assumed to be not only constant in space, but also in time. As discussed in Ho et al. [27] and more recently Schaefer et al. [64], if one wishes to go beyond detection and constrain cosmological models with the ISW, then it is likely that this over simplification will introduce a bias in the recovered parameters, especially when redshift selection functions are broad. The next simplest scenario is a time-dependent linear relationship:

$$\delta_\alpha(\mathbf{x}, a) = b_1^\alpha(a)\delta(\mathbf{x}, a) \ , \tag{61}$$

where $\delta_\alpha \to \{\mathrm{g}, \mathrm{h}, \mathrm{c}, \dots\}$ denotes the tracer type, e.g. galaxies, haloes, clusters etc., $b_1^\alpha(a)$ is a linear bias parameter that varies in time but is independent of scale. In this case the ISW cross-spectra and biased tracer auto-spectra may be easily computed as (cf. Eq. 31):

$$P^{\rm Lin}_{\alpha\dot{\Phi}}(k) = b_1^\alpha(a)\mathcal{F}(k)\left[\frac{H(a)}{a}\left(1 - f(a)\right)\right] P^{\rm Lin}_{\delta\delta}(k;t) \tag{62}$$

$$P^{\rm Lin}_{\alpha\alpha}(k) = [b_1^\alpha(a)]^2 P^{\rm Lin}_{\delta\delta}(k;t) \ . \tag{63}$$

B. Nonlinear theory for the bias

Several recent theoretical and numerical studies of the bias of dark matter haloes [54, 57, 65], have revealed that the linear model is only likely correct on asymptotically large scales. These predictions have been confirmed by several observational studies of the relative bias of different galaxy populations [66–68]. In Smith et al. [54] it was shown that the scale dependence of halo bias was a strong function of scale for $k > 0.07\,h\,\mathrm{Mpc}^{-1}$. In that work a physically motivated analytic framework was developed to model these scale changes. A similar approach was independently developed by [69, 70]. The model utilizes a nonlinear local bias model [71, 72]:

$$\delta_\alpha(\mathbf{x}, a) = \sum_{n=1}^{\infty} \frac{b_n^\alpha(a)}{n!}\left[\delta^n(\mathbf{x}, a) - \langle\delta^n(\mathbf{x})\rangle\right] \ , \tag{64}$$

where the constant term from the Taylor expansion was rewritten as $b_0^\alpha = -\sum_{j=1} b_j^\alpha(a)\left\langle\delta^j\right\rangle/j!$. The density field may be expanded using the PT series expansions from §IV C. As was shown by Smith et al. [54], if one transforms to Fourier space and collects terms to a fixed order, then the density field of the biased tracers may be written as a fluctuation series of the form:

$$\delta^\alpha(\mathbf{k}, a|R) \ = \ \sum_{n=1}^{\infty}[D(a)]^n\left[\delta^\alpha(\mathbf{k}, a|R)\right]_n \ ; \tag{65}$$

$$\left[\delta^\alpha(\mathbf{k}|a, R)\right]_n \ = \ \int \frac{\prod_{i=1}^n\left\{d^3q_i\,\delta_1(\mathbf{q}_i)\right\}}{(2\pi)^{3n-3}}\left[\delta^D(\mathbf{k})\right]_n \times F_n^\alpha(\mathbf{q}_1, ..., \mathbf{q}_n|a, R) \ , \tag{66}$$

where $\left[\delta^\alpha(\mathbf{k}|a, R)\right]_n$ is the nth order perturbation to the biased tracer density field. The functions $F_n^\alpha(\mathbf{q}_1, ..., \mathbf{q}_n|a, R)$ are the bias tracer PT kernels, symmetrized in all of their arguments. The kernels are described in Smith et al. [54]. Thus equations (65) and (66) can be used to describe the mildly non-linear evolution of the biased fields to arbitrary order in the dark matter perturbation. There is a subtlety that we have skipped over: in order to facilitate the Taylor expansion of the biased field it was necessary to filter on a scale R, and hence all of the kernels depend on the filter scale. To remove the filter dependence we adopt the renormalization scheme suggested by McDonald [69, 70]. The down side of this, is that the parameters may not be derived *ab initio*, but must be obtained through fitting to measured data and we shall do this in the following section.

Using these relations, along with McDonald's renormalizations, we find that the ISW–biased density tracer cross- and auto-power spectra may be written:

$$P^{\rm NL}_{\alpha\dot{\Phi}}(k, a) \ = \ P^{\rm Lin}_{\alpha\dot{\Phi}}(k, a) + P^{\rm 1Loop}_{\alpha\dot{\Phi}}(k, a) \ ; \tag{67}$$

$$P^{\rm NL}_{\alpha\alpha}(k, a) \ = \ P^{\rm Lin}_{\alpha\alpha}(k, a) + P^{\rm 1Loop}_{\alpha\alpha}(k, a) \ , \tag{68}$$

where the loop corrections are given by,

$$P^{\rm 1Loop}_{\alpha\dot{\Phi}} \ = \ \mathcal{F}(k)\frac{H(a)}{a}\left[1 - 2f(a)\right]P^{\rm 1Loop}_{R,\alpha\delta}(k, a) \ ; \tag{69}$$

$$P^{\rm 1Loop}_{\alpha\delta} \ = \ b^\alpha_{R,1}P^{\rm 1Loop}_{\delta\delta} + b^\alpha_{R,2}A(k, a) \ ; \tag{70}$$

$$P^{\rm 1Loop}_{\alpha\alpha} \ = \ 2b^\alpha_{R,1}b^\alpha_{R,2}A(k, a) + \frac{[b^\alpha_{R,2}]^2}{2}B(k, a) + N^\alpha_R(k) \tag{71}$$

and where we have introduced the auxiliary functions:

$$A(k, a) \ \equiv \ \int \frac{d^3q}{(2\pi)^3}\,P_{\rm Lin}(q)P_{\rm Lin}(|\mathbf{k} - \mathbf{q}|)F_2(\mathbf{q}, \mathbf{k} - \mathbf{q}) \tag{72}$$

$$B(k, a) \ \equiv \ \int \frac{d^3q}{(2\pi)^3}\,P_{\rm Lin}(q)\left[P_{\rm Lin}(|\mathbf{k} - \mathbf{q}|) - P_{\rm Lin}(q)\right] \tag{73}$$

TABLE II: Halo mass classes, and number densities.

	Mass Range $[\times 10^{13} h^{-1} M_\odot]$	$\bar{n}(z=0)$ $[h^{-1}\mathrm{Mpc}]^3$	$\bar{n}(z=1)$ $[h^{-1}\mathrm{Mpc}]^3$
Bin 1	$[1.50 < M < 10.0]$	3.5×10^{-4}	1.8×10^{-4}
Bin 2	$[10.0 < M]$	2.5×10^{-5}	3.3×10^{-6}

In the above equations we introduced the renormalized bias parameters $b^{\alpha}_{R,i}(a)$ and the renormalized constant power term $N^{\alpha}_{R}(a)$. This may be thought of as an arbitrary white noise contribution.

Before moving on, we notice that the sign reversal property of the nonlinear cross-power spectrum of $\dot{\Phi}$ with mass density, remains unchanged. This owes to the fact that $b_{R,2}$ changes the scale at which the loop corrections transit from large-scale power suppression to small-scale enhancement (provided loop corrections are small compared to linear theory).

C. Renormalized halo bias parameters

In order to use the nonlinear bias model we require the time evolution of the bias parameters, b_1 and b_2. These can be estimated directly from the simulations in the following way. Firstly, we divided the haloes at each expansion factor into two classes: (Bin 1) group scale dark matter haloes and (Bin 2) cluster scale dark matter haloes (see Table II for details).

These mass bins can be faithfully traced within our simulations out to $z = 1$. We choose fixed mass bins at all epochs for simplicity, but a reasonable association can be made between these halo bins and tracer populations such as Luminous Red Galaxies (LRGs) or clusters. Then for each realization we compute the power spectra: $P_{\rm hh}$, $P_{{\rm h}\delta}$, $P_{{\rm h}\omega}$, and $P_{{\rm h}\dot{\Phi}}$, for all of the snapshots from $z = [0, 1]$. The renormalized halo bias parameters were then directly estimated from the $P_{{\rm h}\delta}$ data in the following fashion. Firstly, we fit for $b^{\rm h}_{R,1}$ on the largest scales using an inverse variance estimator of the form:

$$\hat{b}^{\rm h}_{R,1} = \frac{\sum_{i\in[k_1,k_2]} \hat{b}^{\rm h}_1(k_i)/\sigma^2_{b_1}(k_i)}{\sum_{i\in[k_1,k_2]} 1/\sigma^2_{b_1}(k_i)} \; ; \qquad (74)$$

$$\sigma^2_{b_1} = \sum_{i\in[k_1,k_2]} 1/\sigma^2_{b_1}(k_i) \; , \qquad (75)$$

where $\hat{b}^{\rm h}_1(k_i) = \hat{P}_{{\rm h}\delta,i}/\hat{P}_{\delta\delta,i}$ and with $[k_1, k_2] = [0.0, 0.05]\, h\,\mathrm{Mpc}^{-1}$. Note that we assume that there is little covariances between k bins on these large scales. Having obtained $b^{\rm h}_{R,1}$, we next obtain our estimate for $b^{\rm h}_{R,2}$. Our estimator has exactly the same form as the above equations except for the fact that $b^{\rm h}_{R,1} \to b^{\rm h}_{R,2}$ and $\sigma_{b_1} \to \sigma_{b_2}$ and that $[k_1, k_2] = [0.05, 0.2]\, h\,\mathrm{Mpc}^{-1}$. The important quantity to specify is,

$$\hat{b}^{\rm h}_2(k_i) = \frac{1}{A(k_i)}\left[\hat{P}_{{\rm h}\delta,i} - \hat{b}^{\rm h}_{R,1} P_{\delta\delta}(k_i)\right] \; . \qquad (76)$$

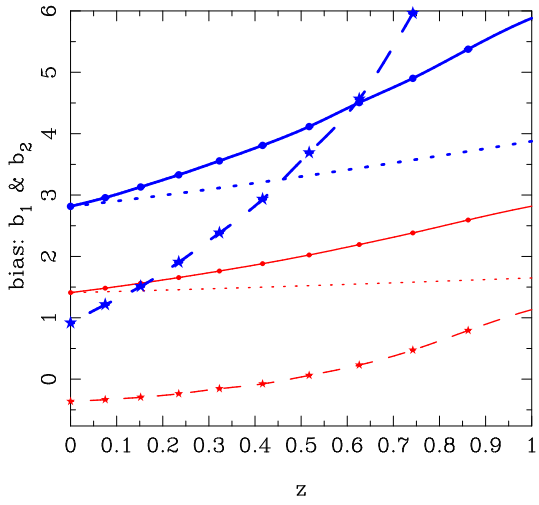

FIG. 10: Renormalized bias parameters $b_{R,1}$ and $b_{R,2}$ as a function of redshift. Red (thin) and blue (thick) lines and points denote results from Bin 1 and Bin 2, respectively. The symbols are: $b_{R,1}$ estimates – solid points; $b_{R,2}$ estimates – stars. The dotted lines show the bias evolution model of Eq. (78).

It will also be useful later on for us to predict $P_{\rm hh}$, and to do this we are required to additionally estimate the renormalized shot noise term: $N^{\rm h}_R(a)$. This may be obtained directly from our estimates of $\hat{P}_{{\rm hh},i}$ along with Eq. (68) and by using Eq. (74), but with $b^{\rm h}_{R,1} \to N^{\rm h}_R$ and $\sigma_{b_1} \to \sigma_{N^{\rm h}}$ and with $[k_1, k_2] = [0.0, 0.2]\, h\,\mathrm{Mpc}^{-1}$. Our estimate per mode is

$$\hat{N}^{\rm h}_R = \hat{P}_{{\rm hh},i} - [\hat{b}^{\rm h}_{R,1}]^2 P_{\delta\delta}(k_i) - [\hat{b}^{\rm h}_{R,2}]^2 B(k_i) - 2\hat{b}^{\rm h}_{R,1}\hat{b}^{\rm h}_{R,2} A(k_i) \; . \qquad (77)$$

Fig. 10 shows the time evolution of the best fit renormalized halo bias parameters. As is evident from the figure, the values of $b^{\rm h}_{R,1}$ for the two samples decrease with increasing time. This is qualitatively consistent with the halo bias evolution that emerges from Extended Press-Schechter formalism and the Peak-background split argument (dotted lines), where linear halo bias decays with time as [73–75]:

$$[b_1(a) - 1] = D(a_0)/D(a)\,[b_1(a_0) - 1] \; . \qquad (78)$$

However as the figure clearly shows the actual measured halo bias evolves much more strongly as a function of redshift. We also note that the values of $b^{\rm h}_{R,2}$ are also similarly consistent with this theory, which predicts that $b^{\rm h}_{R,2} < 0$ for haloes around $M_*(t)$ (the characteristic nonlinear halo mass at that epoch $\sigma(M_*, t) = 1$), and that $b^{\rm h}_{R,2} > 0$ for haloes with $M > M_*(t)$ [76].

D. Results: Evolution of halo–density spectra

Fig. 11 shows the evolution of $P_{{\rm h}\delta}$ in the simulations. The left panel presents the results for haloes in

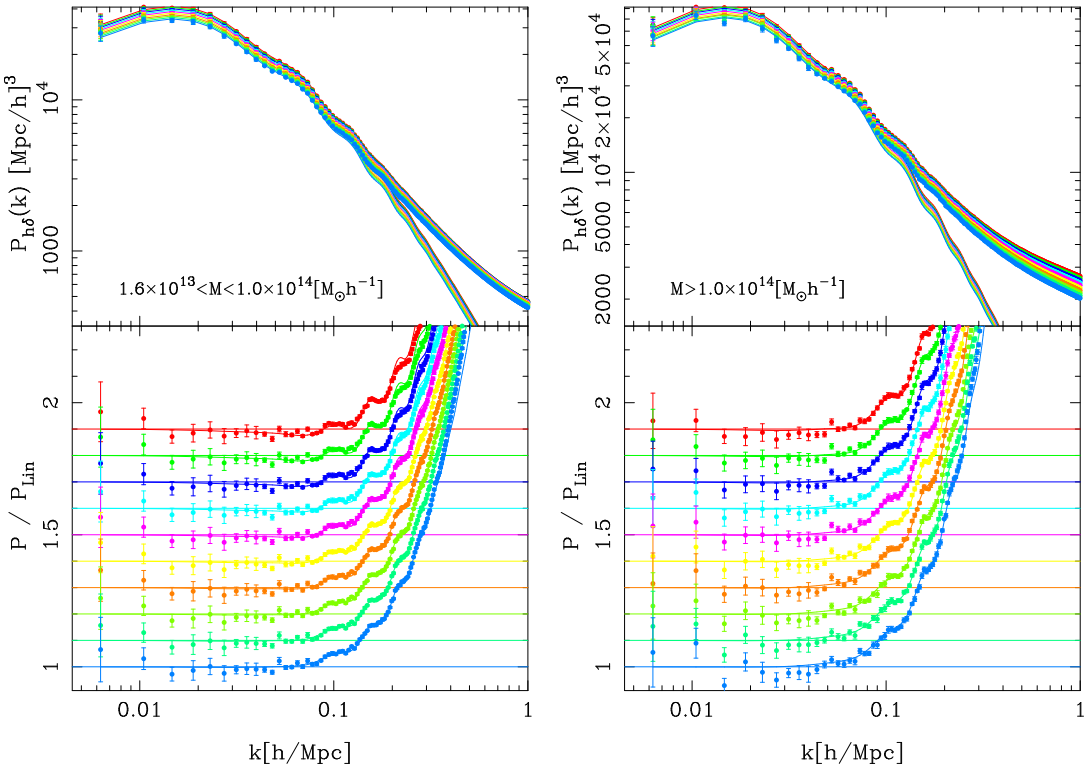

FIG. 11: Evolution of the h–δ cross-power spectra as a function of spatial wavenumber from $z = 1$ to 0. Left panel is for haloes in Bin 1 and the right panel shows results for haloes in Bin 2. Points and lines are as presented in Fig. 3.

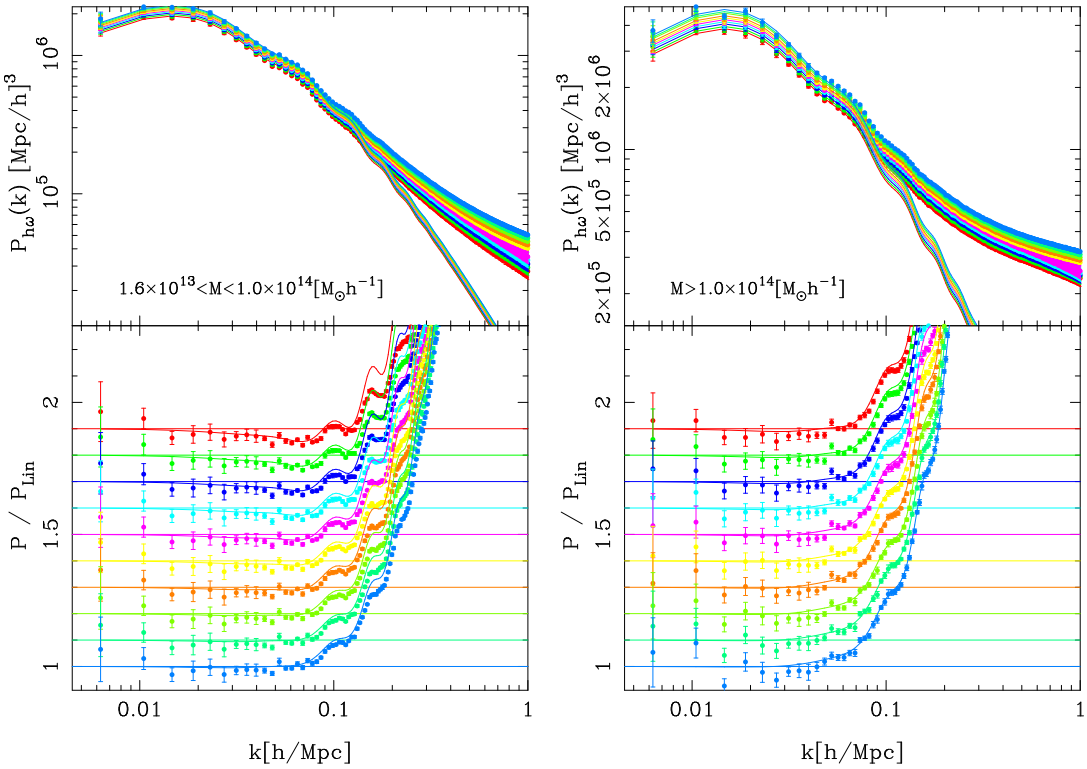

FIG. 12: Evolution of the h-ω cross-power spectra as a function of spatial wavenumber from $z = 1$ to 0. Left panel is for haloes in Bin 1 and the right panel shows results for haloes in Bin 2. Points and lines are as presented in Fig. 3

Bin 1 and the right Bin 2. The top sections show the absolute power and the lower sections show the ratio with respect to the linear theory predictions. We observe that all spectra exhibit a strong scale dependence relative to the linear theory and that the departure is characterized by a suppression of power on large scales ($k > 0.05\,h\,\mathrm{Mpc}^{-1}$) followed by power amplification on smaller scales ($k > 0.1\,h\,\mathrm{Mpc}^{-1}$), and this is exhibited in both mass bins and at all times. The highest mass bin exhibits the strongest amplification with scale, by $k \sim 0.1\,h\,\mathrm{Mpc}^{-1}$ the spectra are 10% in excess of the linear theory, whereas Bin 1 shows a slightly stronger large-scale power suppression. In the lower sections of each panel in Fig. 11 we also show the predictions of the nonlinear renormalized bias model from § VII B and we find surprisingly good agreement over all of the scales of interest. We note that for Bin 1 on the smallest scales $k > 0.5\,h\,\mathrm{Mpc}^{-1}$, the predictions appear to drop dramatically to zero. However, for the computation of the C_l we expect that this theoretical accuracy will be sufficient. This owes to the fact that the spectra shown in Fig. 11 will all be premultiplied by $\mathcal{F}(k) \propto k^{-2}$ and so will be suppressed relative to larger scales. We note that the scale dependence of the halo cross-power spectra were investigated by Smith et al. [54] and we confirm the basic results presented in that study.

E. Results: Evolution of halo–momentum spectra

Fig. 12 shows the evolution of the halo–pseudo-momentum cross-power spectra as a function of scale. Again left and right panels are for Bins 1 and 2, respectively. As expected from our investigation of $P_{\delta\omega}$, we again see nonlinear features in these spectra, and that they are more enhanced relative to those in the $P_{\mathrm{h}\delta}$ spectra. This can be inferred through considering the ratios of the spectra with respect to linear theory (bottom section of each panel). In particular, we note that for Bin 1 and the $z = 0$ snapshot, the large-scale suppression feature is of the order $\sim 5\%$ at $k \sim 0.7\,h\,\mathrm{Mpc}^{-1}$, in contrast to $\sim 2\%$ supression in $P_{\mathrm{h}\delta}$. Again, in the lower panels we over plot the predictions from the renormalized bias model and the agreement is again good, although for $k > 0.2\,h\,\mathrm{Mpc}^{-1}$ small deviations of the model from the data are more apparent. Also, the predictions for Bin 1 drop to zero at higher k, and this occurs for the reasons previously noted.

F. Results: Evolution of halo–$\dot{\Phi}$ spectra

In Fig. 13 we combine the power spectra from the previous two subsections to explore the evolution of $P_{\mathrm{h}\dot{\Phi}}$. As was done for the analysis of $P_{\dot{\Phi}\dot{\Phi}}$ and $P_{\delta\dot{\Phi}}$ we introduce a dimensionless and scaled form of the biased cross-power spectrum (c.f. Eq. 45):

$$\Delta^2_{\mathrm{h}\dot{\Phi}}(k) = \frac{k^3}{2\pi^2}\left[P_{\mathrm{h}\delta}(k) - \frac{P_{\mathrm{h}\omega}(k)}{H(a)a(t)}\right] . \qquad (79)$$

The top panels compare the spectra estimated from the simulations (points with error bars) and the linear theory predictions (solid lines). The lower panels show the ratio with respect to the linear predictions, and the lines show the predictions from the renormalized nonlinear bias model. As was the case for our investigation of $\Delta^2_{\dot{\Phi}\delta}$ (c.f. VI B), departures from linear theory are increasingly apparent as one considers higher redshifts. In addition, there is a sign change in the spectra as one goes from low to high k. The explanation again follows our earlier discussions surrounding Figs 6 and 9. On comparing these results for the haloes with those for the dark matter, Fig. 9, we find that the scale at which the spectra switch sign becomes larger with increasing bias.

Considering the small-scale, late-time ISW boost relative to linear theory, we see that for the haloes at $z = 0$ the signal is stronger as bias increases. However, we also note that the amplification is present for the Bin 1 halo sample by $z \sim 0.3$, compared to the Bin 2 sample where it is absent by $z > 0.1$. This result means that, at late times in LCDM model, nonlinear evolution can *enhance* the decay of gravitational potentials and that the rate of decay also depends on the environment. Again, this result naturally emerges from the PT (c.f. §IV C), although as is shown in the figure, the PT struggles to capture the measured spectra precisely. In the next section we shall investigate whether these nonlinear effects are sufficiently large to impact the ISW-density tracer C_l's.

VIII. CMB-LSS ANGULAR POWER SPECTRUM

A. Theory

We now turn to the calculation of the ISW–biased density tracer angular power spectrum. As described in §V for the ISW auto-spectrum, we may also decompose the projected fluctuations in our biased density tracer into spherical harmonics. To do this, we define the 2D biased density field as the weighted projection of the 3D density field along the line of sight and in a cone of solid angle $d\Omega$. This we may write as,

$$\delta^{\mathrm{2D}}_{\alpha}(\vec{\theta}) = \int_{\chi_i}^{\chi_j} d\chi D_A^2(a) q(\chi) \delta^{\mathrm{3D}}_{\alpha}(D_A(\chi)\vec{\theta}, \chi) , \qquad (80)$$

where $q(\chi)$ is a radial weight function, which is normalized such that

$$\int_{\chi_i}^{\chi_j} d\chi 4\pi D_A^2(\chi) q(\chi) = 1 . \qquad (81)$$

To proceed we must specify $q(\chi)$. For a typical magnitude limited survey the weight function would be

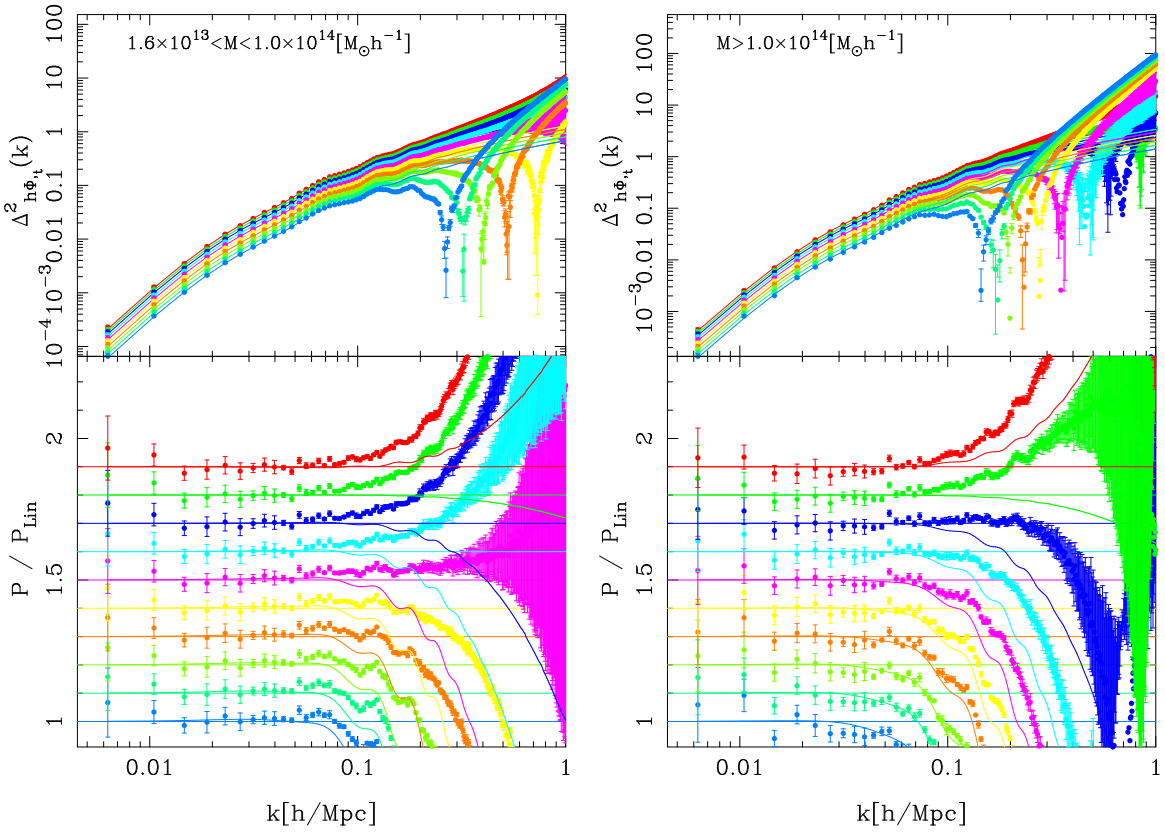

FIG. 13: Evolution of the dimensionless scaled h-$\dot{\Phi}$ cross-power spectra ($\Delta^2_{\mathrm{h}\dot{\Phi}}$) as a function of wavenumber from $z = 1$ to 0. Left and right panels show results for haloes in Bin 1 and Bin 2, respectively. Points and lines are as presented in Fig. 3.

$q(\chi) = n(> L_\chi)/N_{\rm TOT}$ where $n(> L_\chi, \chi)$ is the space density of galaxies above the flux limit at a given redshift, and $N_{\rm TOT}$ is the total number of galaxies, and so $D_A^2(\chi)q(\chi) \propto dN(z)/dz$ the number redshift distribution. Therefore, in turn, one is required to specify a model for the redshift distribution [see for example 21, 22].

Since we are more interested in *precisely* quantifying the importance of nonlinear contributions to the cross-correlation signal for biased tracers, which we can measure directly at all epochs in the simulations, we shall therefore forgo attempting to fabricate certain aspects of a real galaxy survey – this level of detail may confuse interpretation. Instead we shall take a more simplified approach: we assume that, above some fixed mass threshold, there is one and only one galaxy (perhaps an LRG) per dark matter halo; that the mass threshold is independent of redshift; and that we may construct a volume limited sample of these objects from $z = 0$ out to $z = 1$. This last condition implies that there is a tight relation between the mass threshold of the host halo and the luminosity threshold for the carefully selected target galaxy. Our model galaxy survey is therefore equivalent to a target sample of haloes above some fixed mass from redshift $z = 0$ to 1. Hence, we shall write the weight function, $q(\chi) = n(> M, \chi)/N_{\rm TOT}(\chi_i, \chi_j)$, where $n(> M, \chi)$ is the cumulative number density of dark matter haloes with masses greater than M at time $t(\chi)$; and where by our normalization condition, for a redshift shell between z_i and z_j we have

$$N_{\rm TOT}(\chi_i, \chi_j) = \int_{\chi_i}^{\chi_j} d\chi 4\pi D_A^2(\chi) \int_M^\infty dM n(M;\chi) \ . \tag{82}$$

In the above, $n(M, \chi)$, is the differential halo mass function at time $t(\chi)$ and $\chi_i \equiv \chi(z_i)$. Figure 14 shows the redshift distributions of our mock target samples, in the two mass bins and as a function of redshift. In the figure we have introduced the new weight function

$$\Pi_{ij}(\chi) \equiv 4\pi D_A^2(\chi)\Theta_{ij}(\chi) \int_M^\infty dM \frac{n(M,\chi)}{N_{\rm TOT}(\chi_i,\chi_j)} \ , \tag{83}$$

where $\Theta_{ij}(\chi) \equiv [\Theta(\chi - \chi_i) - \Theta(\chi - \chi_j)]$, is the top-hat function with Θ being the Heaviside step function.

The multipole amplitudes of the biased density tracers may therefore be written,

$$a^{\rm h}_{lm} = (-i)^l 4\pi \int \frac{d^3k}{(2\pi)^3} Y^*_{l,m}(\hat{\mathbf{k}}) \Delta^{\rm h}_l(k, \chi_i, \chi_j) \ , \tag{84}$$

with,

$$\Delta^{\rm h}_l(k, \chi_i, \chi_j) \equiv \int_{\chi_i}^{\chi_j} d\chi \Pi_{ij}(\chi) j_l(k\chi) \delta^{\rm 3D}_{\rm h}(k, \chi) \ . \tag{85}$$

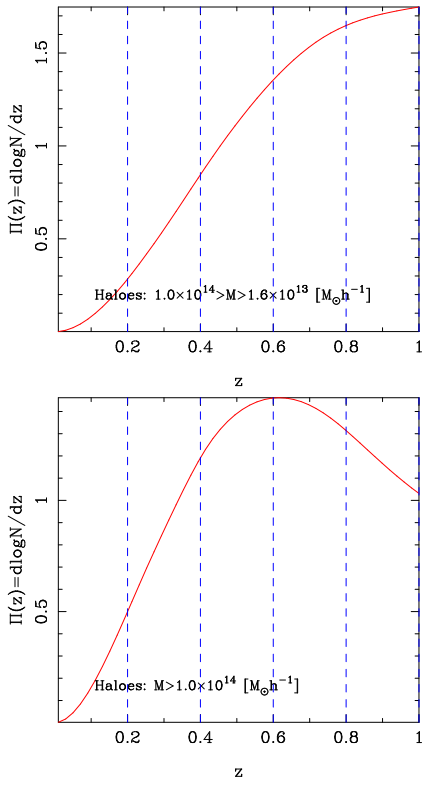

FIG. 14: Mock LRG/cluster normalized number redshift distributions as a function of redshift. Top panel shows results for intermediate mass host haloes (Bin 1), and lower panel results for cluster mass host haloes (Bin 2). Note that here we show the normalized distributions over the entire sample range $z = 0$–1. The blue vertical dash lines show the 5 redshift bands for which we compute the cross-correlations, and note that we renormalize the distribution for each band.

Following Eq. (49), the cross-angular-power of the ISW temperature fluctuations and the projected density tracers may then be written:

$$C_l^{\mathrm{h}T} = \frac{2}{\pi}\int dk k^2 \int_0^{\chi_{\rm max}} d\chi_1 d\chi_2 j_l(k\chi_1) j_l(k\chi_2) \times \frac{2a_1}{c^3}\Pi_{ij}(\chi) P_{\mathrm{h}\dot{\Phi}}(k;\chi_1,\chi_2)\ . \quad (86)$$

Under the Limber approximation (c.f. §V) this expression reduces to:

$$C_l^{\mathrm{h}T} \approx \int_0^{\chi_{\rm max}} d\chi \frac{2a}{c^3}\Pi_{ij}(\chi) P_{\mathrm{h}\dot{\Phi}}\left(k=\frac{l}{D_A(\chi)},\chi\right)\frac{1}{\chi^2}\ ; \approx \frac{2}{c^2}\int_{a(\chi_{\rm max})}^{a_0} d\ln a\, \Pi_{ij}(a) P_{\mathrm{h}\dot{\Phi}}\left(k=\frac{l}{D_A(a)},a\right) \times \frac{1}{H(a)\chi^2(a)}\ ; \quad (87)$$

and for the halo auto-power spectrum we have

$$C_l^{\mathrm{hh}} \approx \int_{a(\chi_{\rm max})}^{a_0} d\ln a\, \Pi_{ij}^2(a) P_{\mathrm{hh}}\left(k=\frac{l}{D_A(a)},a\right) \times \frac{1}{H(a)\chi^2(a)}\ . \quad (88)$$

In Appendix A we present a short investigation of the validity of the Limber approximation for predicting the ISW-LSS cross-power spectrum. There we show that the relative error is $< 10\%$ for $l \sim 10$ and that for $l > 10$ it is $< 2\%$, and for a wide range of survey window functions. These results are consistent with the findings of Rassat et al. [25] for the 2MASS survey. Since we are interested in scales $l > 10$, we shall therefore use the Limber approximated expressions.

B. Results: ISW–biased tracer angular spectrum

Figure 15 presents the results for the angular cross power spectrum for the ISW and haloes in Bin 1 (left panel) and haloes in Bin 2 (right panel). In each case we show the results for 5 narrow bins in redshift, and where for each bin we weight by the redshift distributions presented in Fig. 14. The solid green lines in the figure denote the linear bias predictions; the red dashed lines correspond to our predictions from the nonlinear renormalized PT, as described in §VII B and §VII C; and the blue triple-dot dash lines correspond to our bi-cubic spline fit to the ensemble average measurements of $P_{\mathrm{h}\dot{\Phi}}$ from the simulations, and scaled by linear theory.

In the figure we see that for both Bins 1 and 2 the peak of the angular power spectrum moves to the right and upwards as the mean redshift of the sample increases. The rightward shift is due to the fact that for a given physical scale the angular size decreases with distance, in this case the scale is the peak of the $P_{\mathrm{h}\dot{\Phi}}$ spectrum. The upward shift is more complex, if we were considering unbiased tracers then we would expect that the signal would drop with increasing redshift, owing to the fact that the ISW signal switches off and also the amplitude of the power spectrum is decreasing with $D^2(z)$. However, for a fixed mass range, the bias of the sample increases with increasing redshift (c.f. Fig. 10). For the two host halo mass bins that we consider the bias evolves by a factor of ~ 2 from $z = 0$–1.

Regarding the impact of nonlinearity on the predictions, we find that for $l < 100$ these are small, being at most $< 10\%$. For Bin 1, the deviations are characterized by a several percent boost around $l = 50$, followed by a several percent suppression by $l = 100$. Whereas for Bin 2, the deviations are represented as a few percent suppression. For $l > 100$ the deviations are, in all but one case, characterized by a much more significant suppression, and the signal rapidly drops to zero. The case which does not conform to this picture is the lowest redshift slice for Bin 1, here the signal estimated from the

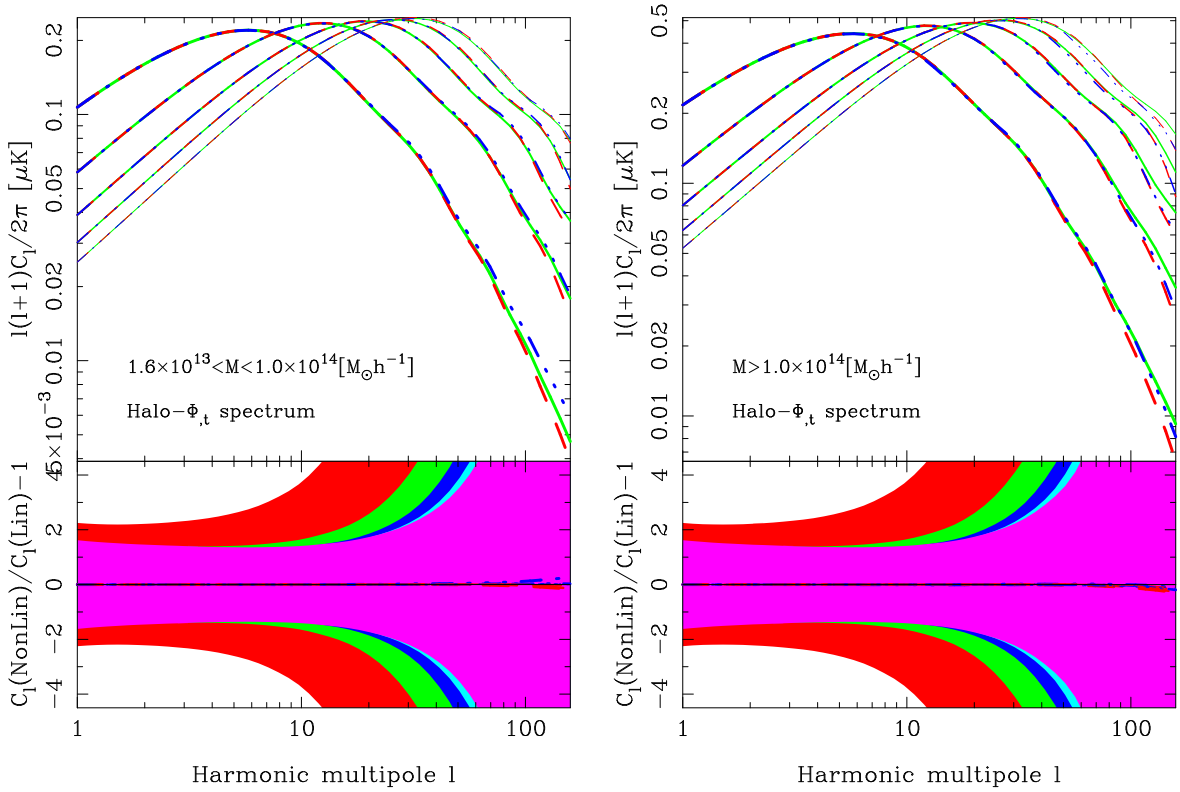

FIG. 15: Angular cross-power spectrum of ISW effect and haloes as a function of spherical harmonic multipole l. *Left panel*: results for group scale dark matter haloes. *Right panel*: results for the most massive clusters. In each panel we show results for 5 equally spaced bins in redshift over the range: $z = [0.0, 1.0]$. The predictions are differentiated by line thickness: thick lines – low redshift; thin lines – high. The line styles denote: linear theory – solid green line; nonlinear PT – red dash line; bi-cubic spline fit to the simulation data – blue triple-dot dash line. Top sections of each panel give the absolute power, and the lower sections the ratio with respect to linear theory. The shaded regions represents the 1-σ error domains per multipole of the linear cross-spectra, where the central redshifts $z \in \{0.1, 0.3, 0.5, 0.7, 0.9\}$, correspond to the colours (red, green, blue, cyan, magenta).

simulations appears to be boosted by $\sim 10\%$ at $l \sim 100$. Unfortunately, this amplification is not mirrored in the predictions from the PT, as also seen in Fig (13) for the last four spectra.

In Fig. 15 we also show the expected 1–σ error domains (shaded regions) of the cross-spectra, computed from using the simple variance formula:

$$\Delta^2\big(C_l^{\rm Th}\big) = \frac{1}{f_{\rm sky}}\frac{1}{(2l+1)}\left[C_l^{\rm hh}C_l^{TT} + \big(C_l^{\rm Th}\big)^2\right] \ . \quad (89)$$

As in the case for C_l^{TT}, we again find that the cosmic and sample variance errors dominate over the modeling errors on scales $l < 100$.

C. Calculation of the $\mathcal{S}/\mathcal{N}$ for biased tracers

The result from Hernández-Monteagudo [29] is that for the ISW–dark matter cross-correlation up to 90% of the Signal-to-Noise ($\mathcal{S}/\mathcal{N}$) for the ISW comes from harmonic modes $l < 50$. Here we shall assess whether sampling biased density tracers can change these conclusions. From the last equation we write the $\mathcal{S}/\mathcal{N}$ for the ISW–dark matter cross-correlation, at a given multipole l, as

$$(\mathcal{S}/\mathcal{N})_l^2 = f_{\rm sky}(2l+1)\left[\frac{\big(C_l^{T\delta}\big)^2}{C_l^{TT}C_l^{\delta\delta} + \big(C_l^{T\delta}\big)^2}\right] \ . \quad (90)$$

Similarly, this equation can be written for the halo distribution,

$$(\mathcal{S}/\mathcal{N})_l^2 = f_{\rm sky}(2l+1)\left[\frac{\big(C_l^{\rm Th}\big)^2}{C_l^{TT}C_l^{\rm hh} + \big(C_l^{\rm Th}\big)^2}\right] \ . \quad (91)$$

In the above, no shot noise subtraction on the halo auto-power spectrum is assumed. We can define the cumulative $\mathcal{S}/\mathcal{N}$ below a given multipole l as

$$(\mathcal{S}/\mathcal{N})\,[<l] = \sqrt{\sum_{l'=2}^{l}(\mathcal{S}/\mathcal{N})_{l'}^2}. \quad (92)$$

This addition is legitimate only under full sky coverage ($f_{\rm sky} = 1$), since we assume that different multipoles are

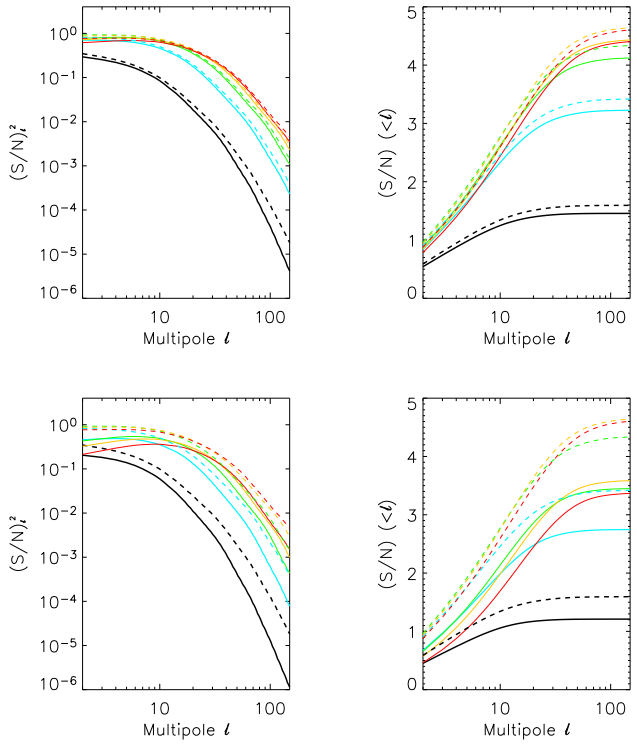

FIG. 16: Top and bottom panels, $\mathcal{S}/\mathcal{N}$ results for Bins 1 and 2, respectively. Left panels: Squared S/N for each multipole l of the cross correlation of the CMB temperature with the most massive (Bin 2) halo population (solid lines) and the total matter density field (dashed lines). Results for different snapshots centered at $z = 0.1$, 0.3, 0.5, 0.7 and 0.9 are displayed in black, blue, green, red and orange colors, respectively. Line thickness decreases with increasing redshift. Right panels: cumulative S/N. Lines are as in left panel.

independent. In the left panel of Fig. 16 we show $(\mathcal{S}/\mathcal{N})_l^2$, for the cluster-mass halo population (Bin 2, solid lines) and the matter density field (dashed lines) for the 5 different redshift shells. The right panel of the figure shows the corresponding cumulative $\mathcal{S}/\mathcal{N}$ below each multipole l. We note that the $(\mathcal{S}/\mathcal{N})_l^2$ is flat for low multipoles, and declines rapidly with increasing l. The scale at which the turn down occurs is a function of redshift. For $z = 0.7$ the turn down occurs at $l < 20$, whereas for $z = 0.1$ it has dropped by $l \sim 10$. From studying the cumulative $\mathcal{S}/\mathcal{N}$, we find that roughly 50% of the total $\mathcal{S}/\mathcal{N}$ is achieved by $l \sim 10$, and that $\sim 90\%$ is achieved by $l \approx 40$ [c.f. 29]. On comparing these results with the corresponding ones for the matter field (dashed lines), we find slightly lower values for the haloes. This may be atributed to the additional Poisson noise. Note that the redshift shell that gives the highest $\mathcal{S}/\mathcal{N}$ is located at $z = 0.7$, and that the total $\mathcal{S}/\mathcal{N}$ for it is of order ~ 7.

Based on these findings, we conclude that it is highly unlikely that nonlinear evolution of the mass distribution or nonlinearities in the scale dependence of bias can significantly affect the detectability of the ISW.

D. Results: Cross-correlation coefficient

Finally, we investigate the cross-correlation coefficient of the CMB temperature fluctuations and the halo samples. The cross-correlation coefficient of two fields A and B is defined as,

$$r_l^{AB} \equiv \frac{C_l^{AB}}{\sqrt{C_l^{AA} C_l^{BB}}} \ . \tag{93}$$

Under the assumption of time independent linear bias we would have $r^{\rm Th} \to r^{T\delta}$. Thus $r_l^{\rm Th}$ does not depend on the bias of the tracer sample, nor the amplitude of the primordial power spectrum. Instead it provides direct information on the Dark Energy parameters and the curvature density: $\{\Omega_{DE}, w_0, \Omega_k, \}$. This approach was developed by Giannantonio et al. [26] to obtain cosmological parameter constraints from current CMB and LSS data [see also 77, for an alternate method for removing bias, that uses CMB lensing.].

The validity of this analysis hinges on the fact that $b\sigma_8^2$ cancels out. However, since the bias is in fact time-dependent, we can only have $r^{\rm Th} \approx r^{T\delta}$. Adding to this the fact that the bias is scale-dependent it appears that such an approximation is unlikely to be robust, and especially for LSS surveys with broad selection functions. We may test their conjecture by estimating $r^{\rm Th}$ for several samples of biased tracers, and if we do not find that they match $r^{T\delta}$ within the same redshift shell, then the modeling should be deemed to be insecure. In that case one must include the redshift evolution of the bias, as done by Ho et al. [27] in their analysis of the NVSS sample.

In Fig. 17 we present the measured cross-correlation coefficients for the Bin 1 (left panel) and Bin 2 (right panel) halo samples and for the 5 redshift bins previously considered. The linear theory predictions are represented by the solid green lines and note that for these we use the time-dependent linear bias estimated directly from the simulations. In the figure we also present two different estimates for the full nonlinear cross-correlation coefficieinent, estimated from bicubic spline fits to the measured spectra: the blue triple-dot dash curves show the results for the case where no shot noise subtraction was performed on the $C_l^{\rm hh}$ data; the red dash curves show the same but with the shot noise subtracted. We also show the dark matter-CMB cross-correlation coefficient, $r^{T\delta}$, measured in the same redshift bins as for the haloes (magenta dot-dash curves). For the dark matter estimates, we used the selection function $\Pi_{ij}^{DM}(\chi) = D_A^2(\chi) / \int_{\chi_i}^{\chi_j} d\chi D_A^2(\chi)$.

For these narrow redshift shells, $\Delta z = 0.2$, we find that for linear theory, neglecting the evolution of the bias does not lead to significant errors. This can be seen from the middle panels of the figures, where we plot $r^{\rm Th}/r^{T\delta}$ (solid

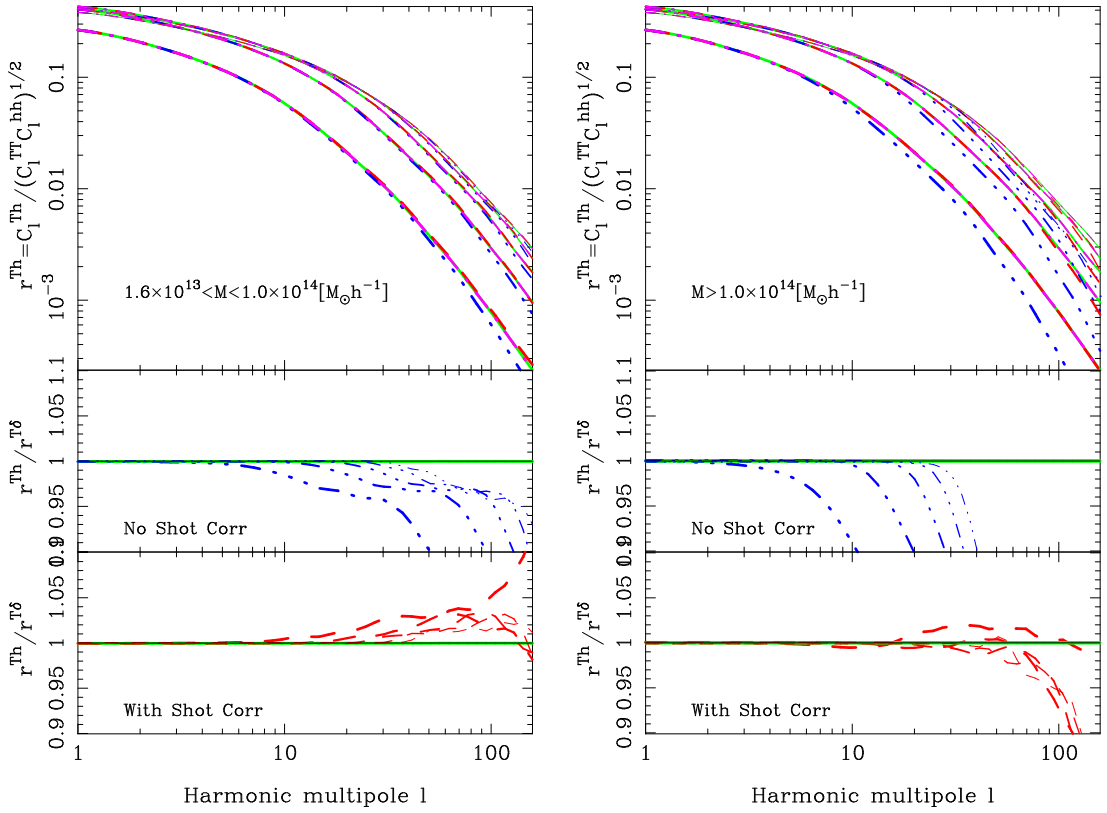

FIG. 17: Cross-correlation coefficient between CMB and haloes (r^{Th}) as a function of harmonic multipole l. Left panel shows results for group-scale haloes and the right for cluster-scale. *Upper panels*: results for 5 redshift bins centred on $z = \{0.1, 0.3, 0.5, 0.7, 0.9\}$ of thickness $\Delta z = 0.2$. Thick to thin lines denote low to high redshift halo samples. Line styles are: green solid line – linear theory; blue triple-dot dash line – bi-cubic spline fit to simulation data without shot-noise subtraction; red dash line the same but with shot-noise subtraction. The magenta dot-dash curve shows the result for the dark matter ($r^{T\delta}$). Middle and lower panels show the ratio of halo to dark matter cross-correlation coefficients without and with shot noise subtraction, respectively.

green line for linear theory). However, for the actual measured nonlinear r^{Th}, we find that the scale-dependence of the C_l^{hh} spectra, leads to a significant discrepancy between r^{Th} and $r^{T\delta}$. The discrepancy is $\approx 10\%$ at $l = 10$ for the lowest redshift cluster-sized halo sample (Bin 2). For the group-scale haloes (Bin 1), the deviation is smaller, being $\approx 10\%$ at $l = 50$, for the same redshif shell. However, if one subtracts shot noise from the halo auto-spectra (bottom panel of the figures), $P_{\rm shot} = 1/\bar{n}_{\rm h}$, then these effects can be mitigated, and the ratio $r^{Th}/r^{T\delta}$ is brought within $5 < \%$ of unity. A cuationary note is that, we found that using the standard $P_{\rm shot} = 1/\bar{n}_{\rm h}$ to correct for the shot-noise lead to negative power spectra at high k. Since this is forbidden, we believe that such simple corrections are in fact an *over-correction* and new more accurate methods for accounting for the discreteness will be required [for a deeper discussion of this issue see 54].

We thus conclude that the relation $r^{Th} \approx r^{T\delta}$ holds to within 5% for $l < 50$, for the halo samples considerd in this study. This comes under the provision that the shot noise is accounted for and the shells are narrow.

IX. CONCLUSIONS

In this paper we have investigated the impact of the nonlinear evolution of the time rate of change of the gravitational potentials on the CMB temperature auto-power spectrum, and also on the cross-correlation of biased density tracers and the CMB. Linear perturbation theory informs us that, for nearly the entire history of the Universe, gravitational potentials are constant and there is no net heating or cooling of the primordial CMB photons. However, at late times in the LCDM model the symmetry between the growth rate of density perturbations and the expansion rate is broken. The growth slows, and potentials begin to decay. Using the `zHORIZON` simulations, a large ensemble of N-body simulations and analytic perturbation theory methods, we explored how this picture changed.

In §III we generated maps of the rate of change of the gravitational potentials at different stages in the simulation. We showed that, at redshifts $z \sim 15 - 10$, whilst the ISW signal is vanishingly small, the potentials are indeed evolving nonlinearly on small scales giving rise to

the Rees-Sciama and Birkinshaw-Gull effects – nonlinear infall and mass motion across the line of sight. However, the amplitude of these effects, at these redshifts, is too low to be detected directly in the CMB or through a cross-correlation analysis. We then showed that at later times $z > 3$ the potential evolution becomes dominated by the large-scale ISW effect.

In §IV we focused on investigating the impact on the CMB temperature power spectrum. The late time ISW effect can be quantified through a line-of-sight integral over three power spectra: the auto-spectra of density and momentum, and their cross-spectrum. We used the nonlinear PT to derive explicit expressions for each of these quantities. Estimates were then measured from the ensemble of simulations over the range $z = 1$–0. In all cases there was evidence for large-scale nonlinearity, the effects being strongest for the momentum auto-spectra and at the lowest redshifts. However, when the spectra were combined to produce the $\dot{\Phi}$ spectrum, the nonlinear corrections to linear predictions increased with increasing redshift. This was attributed to the fact that the ISW vanishes at early times, so leaving only the RS and BG effects. The standard PT was able to reproduce the nonlinear behavior at high precision over this redshift range.

In §V we estimated the CMB spectrum using the Limber approximation, we found that the nonlinear amplification of the ISW effect was $< 10\%$ of the linear theory on scales $l < 50$, and was also swamped by the cosmic variance of the linear ISW effect on these scales. On smaller scales the effect was more significant, however the primary CMB signal is more than $\sim 10^3$ times larger at this scale. We conclude that for the standard LCDM model, it is highly unlikely that the nonlinear ISW effects could contaminate the $l < 1500$ multipoles of the CMB spectrum in any traceable way. Our results support conclusions from earlier studies [11, 15, 17, 78].

In §VI we analyzed the cross-correlation of ISW with the dark matter density field, showing that while the nonlinear effects suppress this cross-correlation at early times, they may enhance it at very late times. This is further investigated in §VII, where we computed the ISW signal obtained from the cross-correlation of the CMB with a set of biased tracers of the density field. We modeled the bias using a time dependent linear model and also a time- and scale-dependent nonlinear model [54, 69, 70]. For the biased samples we took the haloes measured in the simulations between $z = 0$ and 1, with masses $M > 10^{13}h^{-1}M_{\odot}$. These were then sub-divided into a high- and low-mass sample. The linear and nonlinear bias parameters were then estimated from the halo-mass cross-power spectra. The angular power spectrum of the ISW depends on two spectra: the cross-power spectrum of the biased tracer with the mass density and the momentum. These spectra were estimated from the simulations. Again there was evidence for large-scale nonlinearity, the effects being strongest for the momentum cross-spectrum and at late times. The predictions from the nonlinear analytic PT model were found to qualitatively reproduce the power spectra. On combining the two spectra to produce the ISW-density tracer cross-spectrum, we again found evidence of nonlinearity, and as for the case of the ISW auto-spectrum, the effects were more noticeable at higher redshifts. We also found that at late times there was an amplification of the cross-power spectrum. Thus at late times in the LCDM model, nonlinear evolution can lead to a small *increase* in the decay rate of the gravitational potentials.

In §VIII we computed the angular power spectra, averaging over the halo spectra at various redshifts. We found that on scales $l < 100$ the departures from linear theory predictions were $< 10\%$, and these were characterized by a small amplification of the signal, followed by a strong suppression. The departures are sub-dominant to the cosmic variance. We then investigated the $\mathcal{S}/\mathcal{N}$ for the haloes and found good agreement with the linear theory expectation: the presence of bias effectively cancels out in the $\mathcal{S}/\mathcal{N}$ expression and leads to negligible changes in the cross-correlation detectability. We also showed that through the increased Poisson noise of the biased sample, there was a reduction in the $\mathcal{S}/\mathcal{N}$, relative to that for the mass. Our analyses also demonstrated that the $\mathcal{S}/\mathcal{N}$ of the ISW–large-scale structure cross correlation is localized to a narrow angular range: more than $\sim 90\%$ of the overall significance arises from $l < 50$, or angular scales larger than ~ 4 degrees. We therefore conclude that in the current power spectrum analyses of Ho et al. [27] and Giannantonio et al. [26] are not affected by nonlinear density evolution or scale-dependent bias to influence the detectability of the ISW-LSS cross-correlation. Since we do not repeat the exact analysis of Granett et al. [28] we cannot directly address whether that result can be explained by nonlinear effects or whether it requires an alternative explanation.

Finally, we compared the cross-correlation coefficient of the biased density tracers and the CMB with that of the dark matter and the CMB. We found that the relation $r^{T\mathrm{h}} \approx r^{T\delta}$ holds to within 5% for $l < 50$, for the halo samples considerd in this study. This comes under the provision that the shot noise is accounted for and the shells are narrow. Otherwise the deviations can be large.

The power spectrum anslysis of ISW, therefore, appears to be a probe relatively free from contamination by the pernicious effects of late-time nonlinear evolution of the large-scale structures or scale dependent bias, at least for $l < 100$ where most of the signal is. It therefore continues to be a useful probe for the presence of Dark Energy or its alternatives [79].

Acknowledgments

We acknowledge L. Marian for a careful reading of the draft. RES kindly thanks the Argelander Institute, University of Bonn for hospitality whilst some of this work was being performed. CHM acknowledges the warm hospitality of the University of Zurich, where this work was

initiated. We kindly thank V. Springel for making public GADGET-2 and for providing his B-FoF halo finder; R. Scoccimarro for making public his 2LPT code. RES acknowledges support from a Marie Curie Reintegration Grant. This work is partly supported by the Swiss National Foundation under contract 200021-116696/1 and WCU grant R32-2008-000-10130-0.

[1] E. Komatsu, J. Dunkley, M. R. Nolta, C. L. Bennett, B. Gold, G. Hinshaw, N. Jarosik, D. Larson, M. Limon, L. Page, et al., ArXiv e-prints **803** (2008), 0803.0547.
[2] R. K. Sachs and A. M. Wolfe, ApJ **147**, 73 (1967).
[3] M. J. Rees and D. W. Sciama, Nature **217**, 511 (1968).
[4] M. Birkinshaw and S. F. Gull, Nature **302**, 315 (1983).
[5] S. Dodelson, *Modern cosmology* (Modern cosmology / Scott Dodelson. Amsterdam (Netherlands): Academic Press. ISBN 0-12-219141-2, 2003, XIII + 440 p., 2003).
[6] W. Fang, S. Wang, W. Hu, Z. Haiman, L. Hui, and M. May, PRD **78**, 103509 (2008), 0808.2208.
[7] N. Kaiser, MNRAS **198**, 1033 (1982).
[8] E. Martinez-Gonzalez, J. L. Sanz, and J. Silk, ApJL **355**, L5 (1990).
[9] E. Martínez-González, J. L. Sanz, and J. Silk, PRD **46**, 4193 (1992).
[10] E. Martinez-Gonzalez, J. L. Sanz, and J. Silk, ApJ **436**, 1 (1994).
[11] A. Cooray, PRD **65**, 103510 (2002), arXiv:astro-ph/0112408.
[12] A. Cooray, PRD **65**, 083518 (2002), arXiv:astro-ph/0109162.
[13] R. Tuluie and P. Laguna, ApJL **445**, L73 (1995), arXiv:astro-ph/9501059.
[14] R. Tuluie, P. Laguna, and P. Anninos, ApJ **463**, 15 (1996), arXiv:astro-ph/9510019.
[15] U. Seljak, ApJ **460**, 549 (1996), arXiv:astro-ph/9506048.
[16] N. Puchades, M. J. Fullana, J. V. Arnau, and D. Sáez, MNRAS **370**, 1849 (2006), arXiv:astro-ph/0605704.
[17] Y.-C. Cai, S. Cole, A. Jenkins, and C. Frenk, ArXiv e-prints (2008), 0809.4488.
[18] R. G. Crittenden and N. Turok, Physical Review Letters **76**, 575 (1996), arXiv:astro-ph/9510072.
[19] R. Scranton, A. J. Connolly, R. C. Nichol, A. Stebbins, I. Szapudi, D. J. Eisenstein, N. Afshordi, T. Budavari, I. Csabai, J. A. Frieman, et al., ArXiv Astrophysics e-prints (2003), arXiv:astro-ph/0307335.
[20] S. Boughn and R. Crittenden, Nature **427**, 45 (2004), arXiv:astro-ph/0305001.
[21] N. Afshordi, Y.-S. Loh, and M. A. Strauss, PRD **69**, 083524 (2004), arXiv:astro-ph/0308260.
[22] N. Padmanabhan, C. M. Hirata, U. Seljak, D. J. Schlegel, J. Brinkmann, and D. P. Schneider, PRD **72**, 043525 (2005), arXiv:astro-ph/0410360.
[23] A. Cabré, E. Gaztañaga, M. Manera, P. Fosalba, and F. Castander, MNRAS **372**, L23 (2006), arXiv:astro-ph/0603690.
[24] T. Giannantonio, R. G. Crittenden, R. C. Nichol, R. Scranton, G. T. Richards, A. D. Myers, R. J. Brunner, A. G. Gray, A. J. Connolly, and D. P. Schneider, PRD **74**, 063520 (2006), arXiv:astro-ph/0607572.
[25] A. Rassat, K. Land, O. Lahav, and F. B. Abdalla, MNRAS **377**, 1085 (2007), arXiv:astro-ph/0610911.
[26] T. Giannantonio, R. Scranton, R. G. Crittenden, R. C. Nichol, S. P. Boughn, A. D. Myers, and G. T. Richards, PRD **77**, 123520 (2008), 0801.4380.
[27] S. Ho, C. Hirata, N. Padmanabhan, U. Seljak, and N. Bahcall, PRD **78**, 043519 (2008), 0801.0642.
[28] B. R. Granett, M. C. Neyrinck, and I. Szapudi, ApJL **683**, L99 (2008), 0805.3695.
[29] C. Hernández-Monteagudo, A&A **490**, 15 (2008), 0805.3710.
[30] M. Douspis, P. G. Castro, C. Caprini, and N. Aghanim, A&A **485**, 395 (2008), 0802.0983.
[31] M. Frommert, T. A. Enßlin, and F. S. Kitaura, MNRAS **391**, 1315 (2008), 0807.0464.
[32] B. R. Granett, M. C. Neyrinck, and I. Szapudi, ArXiv e-prints (2008), 0812.1025.
[33] L. Verde and D. N. Spergel, PRD **65**, 043007 (2002), arXiv:astro-ph/0108179.
[34] S. Weinberg, *Cosmology* (Cosmology, by Steven Weinberg. ISBN 978-0-19-852682-7. Published by Oxford University Press, Oxford, UK, 2008., 2008).
[35] The Planck Collaboration, ArXiv Astrophysics e-prints (2006), arXiv:astro-ph/0604069.
[36] P. J. E. Peebles, *The large-scale structure of the universe* (Research supported by the National Science Foundation. Princeton, N.J., Princeton University Press, 1980. 435 p., 1980).
[37] V. Springel, MNRAS **364**, 1105 (2005), arXiv:astro-ph/0505010.
[38] D. N. Spergel, L. Verde, H. V. Peiris, E. Komatsu, M. R. Nolta, C. L. Bennett, M. Halpern, G. Hinshaw, N. Jarosik, A. Kogut, et al., ApJS **148**, 175 (2003), arXiv:astro-ph/0302209.
[39] D. N. Spergel, R. Bean, O. Doré, M. R. Nolta, C. L. Bennett, J. Dunkley, G. Hinshaw, N. Jarosik, E. Komatsu, L. Page, et al., ApJS **170**, 377 (2007), arXiv:astro-ph/0603449.
[40] U. Seljak and M. Zaldarriaga, ApJ **469**, 437 (1996), arXiv:astro-ph/9603033.
[41] U. Seljak, N. Sugiyama, M. White, and M. Zaldarriaga, PRD **68**, 083507 (2003), arXiv:astro-ph/0306052.
[42] R. Scoccimarro, MNRAS **299**, 1097 (1998), arXiv:astro-ph/9711187.
[43] M. Crocce, S. Pueblas, and R. Scoccimarro, MNRAS **373**, 369 (2006), arXiv:astro-ph/0606505.
[44] M. Davis, G. Efstathiou, C. S. Frenk, and S. D. M. White, ApJ **292**, 371 (1985).
[45] R. W. Hockney and J. W. Eastwood, *Computer simulation using particles* (Bristol: Hilger, 1988, 1988).
[46] S. Johnson and M. Frigo, http://www.fftw.org/ (2008).
[47] O. Lahav, P. B. Lilje, J. R. Primack, and M. J. Rees, MNRAS **251**, 128 (1991).
[48] J. N. Fry, Physics Letters B **158**, 211 (1985).
[49] A. J. S. Hamilton, MNRAS **322**, 419 (2001), arXiv:astro-ph/0006089.
[50] E. V. Linder and A. Jenkins, MNRAS **346**, 573 (2003), arXiv:astro-ph/0305286.
[51] F. Bernardeau, S. Colombi, E. Gaztañaga, and R. Scoc-

cimarro, Phys. Rep. **367**, 1 (2002), arXiv:astro-ph/0112551.
[52] B. Jain and E. Bertschinger, ApJ **431**, 495 (1994), arXiv:astro-ph/9311070.
[53] R. Scoccimarro and J. A. Frieman, ApJ **473**, 620 (1996), arXiv:astro-ph/9602070.
[54] R. E. Smith, R. Scoccimarro, and R. K. Sheth, PRD **75**, 063512 (2007), arXiv:astro-ph/0609547.
[55] W. H. Press, S. A. Teukolsky, W. T. Vetterling, and B. P. Flannery, *Numerical recipes in FORTRAN. The art of scientific computing* (Cambridge: University Press, —c1992, 2nd ed., 1992).
[56] M. Crocce and R. Scoccimarro, PRD **77**, 023533 (2008), arXiv:0704.2783.
[57] R. E. Angulo, C. M. Baugh, C. S. Frenk, and C. G. Lacey, MNRAS **383**, 755 (2008), arXiv:astro-ph/0702543.
[58] M. Bartelmann and P. Schneider, Phys. Rep. **340**, 291 (2001), arXiv:astro-ph/9912508.
[59] M. Loverde and N. Afshordi, PRD **78**, 123506 (2008), 0809.5112.
[60] U. Seljak and M. Zaldarriaga, PRD **60**, 043504 (1999), arXiv:astro-ph/9811123.
[61] U. Seljak and M. Zaldarriaga, Physical Review Letters **82**, 2636 (1999), arXiv:astro-ph/9810092.
[62] O. Zahn and M. Zaldarriaga, ApJ **653**, 922 (2006), arXiv:astro-ph/0511547.
[63] D. M. Goldberg and D. N. Spergel, PRD **59**, 103002 (1999), arXiv:astro-ph/9811251.
[64] B. M. Schaefer, M. Douspis, and N. Aghanim, ArXiv e-prints (2009), 0903.4288.
[65] S. Cole, A. G. Sanchez, and S. Wilkins, ArXiv Astrophysics e-prints (2006), arXiv:astro-ph/0611178.
[66] W. J. Percival, R. C. Nichol, D. J. Eisenstein, D. H. Weinberg, M. Fukugita, A. C. Pope, D. P. Schneider, A. S. Szalay, M. S. Vogeley, I. Zehavi, et al., ApJ **657**, 51 (2007), arXiv:astro-ph/0608635.
[67] A. G. Sánchez and S. Cole, MNRAS **385**, 830 (2008), 0708.1517.
[68] J. G. Cresswell and W. J. Percival, ArXiv e-prints (2008), 0808.1101.
[69] P. McDonald, PRD **74**, 103512 (2006), arXiv:astro-ph/0609413.
[70] P. McDonald, PRD **74**, 129901 (2006).
[71] J. N. Fry and E. Gaztanaga, ApJ **413**, 447 (1993), arXiv:astro-ph/9302009.
[72] P. Coles, MNRAS **262**, 1065 (1993).
[73] J. N. Fry, ApJL **461**, L65+ (1996).
[74] M. Tegmark and P. J. E. Peebles, ApJL **500**, L79+ (1998), arXiv:astro-ph/9804067.
[75] R. K. Sheth and G. Tormen, MNRAS **308**, 119 (1999), arXiv:astro-ph/9901122.
[76] R. Scoccimarro, R. K. Sheth, L. Hui, and B. Jain, ApJ **546**, 20 (2001), arXiv:astro-ph/0006319.
[77] P. Zhang, ApJ **647**, 55 (2006), arXiv:astro-ph/0512422.
[78] M. Maturi, K. Dolag, A. Waelkens, V. Springel, and T. Enßlin, A&A **476**, 83 (2007), 0708.1881.
[79] L. Lombriser, W. Hu, W. Fang, and U. Seljak, ArXiv e-prints (2009), 0905.1112.

APPENDIX A: VALIDITY OF THE LIMBER APPROXIMATION

The Limber approximation is motivated by:

$$\int_0^\infty dk\; k^2 j_l(kr_1) j_l(kr_2) = \frac{\pi}{2}\frac{\delta^D(r_1-r_2)}{r_1^2}, \qquad \text{(A1)}$$

where the symbol δ^D denotes the Dirac delta function. Under the assumption that the spherical Bessel functions $j_l(kr)$ are rapidly oscillating for high enough l-s, then one can write an integral over a generic power spectrum as

$$\begin{aligned}\mathcal{F}(l,\alpha,r_1,r_2) &\equiv \int_{k_{min}}^{k_{max}} dk\; k^2 j_l(kr_1) j_l(kr_2)\; P(k) \\ &\approx \frac{\pi}{2}\frac{\delta^D(r_1-r_2)}{r_1^2}\; P\left(k=\frac{l+1/2}{r_1}\right) \qquad \text{(A2)}\end{aligned}$$

where the power spectrum $P(k)$ is assumed, in a cosmological context, to be a power law times some transfer function $|T(k)|^2$, $P(k) = k^\alpha |T(k)|^2$. If seen as a four dimensional matrix with indices running on $\{l, \alpha, r_1, r_2\}$, the deviation of $\mathcal{F}$ from a diagonal matrix in the last two indices, may be viewed as a measure of the error introduced by the Limber approximation.

In Fig. 18 we examine $\mathcal{F}$ for the case where we have fixed r_1 to be the comoving distance to $z_0 = 0.4$ and where r_2 varies on the X-axis. We consider three cases for the multipole number: $l = \{4, 38, 103\}$; and three cases for the spectral index: $\alpha = \{1, -1, -3\}$ which may be thought of as $P_{\delta\delta}$, $P_{\dot\Phi\delta}$, and $P_{\dot\Phi\dot\Phi}$. We take $k_{\rm min} = 10^{-5}\,h\,{\rm Mpc}^{-1}$ and $k_{\rm max} = 1\,h\,{\rm Mpc}^{-1}$. For the sake of clarity, the elements of $\mathcal{F}$ have been normalized by the maximum value of each row. Black points denote positive values and green ones negative entries. The diagonal term (at $z_0 = 0.4$) has been marked by a vertical dashed line. From the figure it is clear that the deviation from a diagonal matrix is more apparent at low multipoles, and for more negative values of α. At higher l, however, the width of the $\mathcal{F}$ matrix shrinks around z_0, making the Limber approximation more precise. The actual error on these multipoles is related to how the off-diagonal terms are weighted by the time dependent factors, and how their sum cancels within the integration range.

Fig. 19 presents the errors on $C_l^{\delta\delta}$ and $C_l^{T\delta}$, at three different redshifts $z_0 = \{0.2, 0.4, 0.6\}$ and for thin (green color) and thick (red color) redshift shells (these are displayed in the bottom panels). In all cases, for $l > 20$, the errors are below 3%. We find that for $C_l^{\delta\delta}$, the net resulting error is larger for thin redshift shells than thick ones. This is inverted for $C_l^{T\delta}$, where the contribution to the off-diagonal terms are smaller for thin shells. However errors remain always below the few-percent level. The amplitude of the errors are defined by: the actual width of the peak around $z = z_0$; the amplitude of the oscillating floor around the wings of the peak at $z = z_0$; and the actual width of the redshift integration range compared to the width of the peak at $z = z_0$.

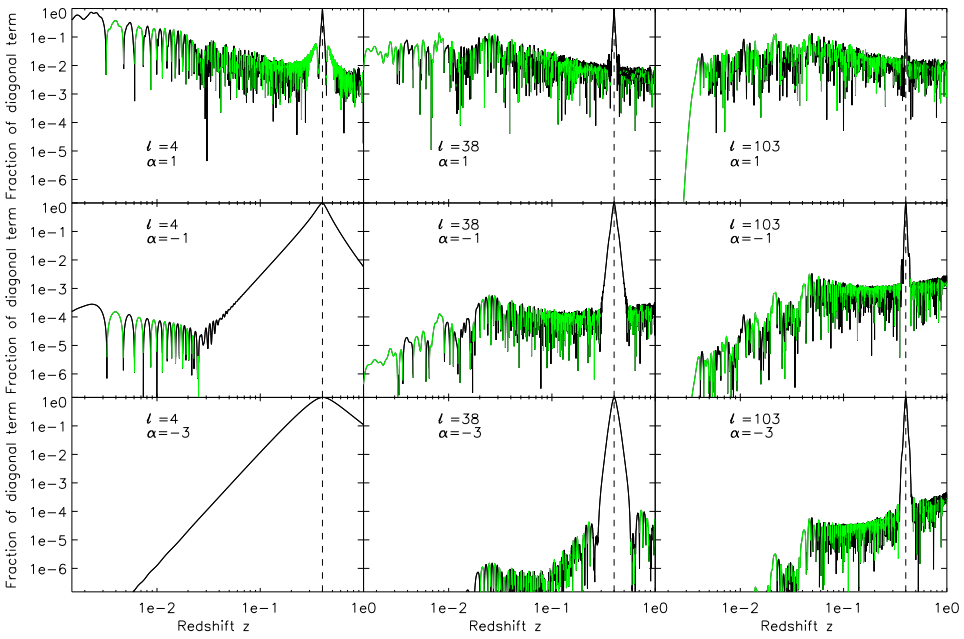

FIG. 18: Rows of the matrix $\mathcal{F}(l, \alpha, r_1, r_2)$ (normalized by the diagonal term) corresponding to $r_1(z_0 = 0.4)$ versus the redshift corresponding to r_2, under different choices of l and α. Given the logarithmic scale, green color displays negative values, black points positive ones.

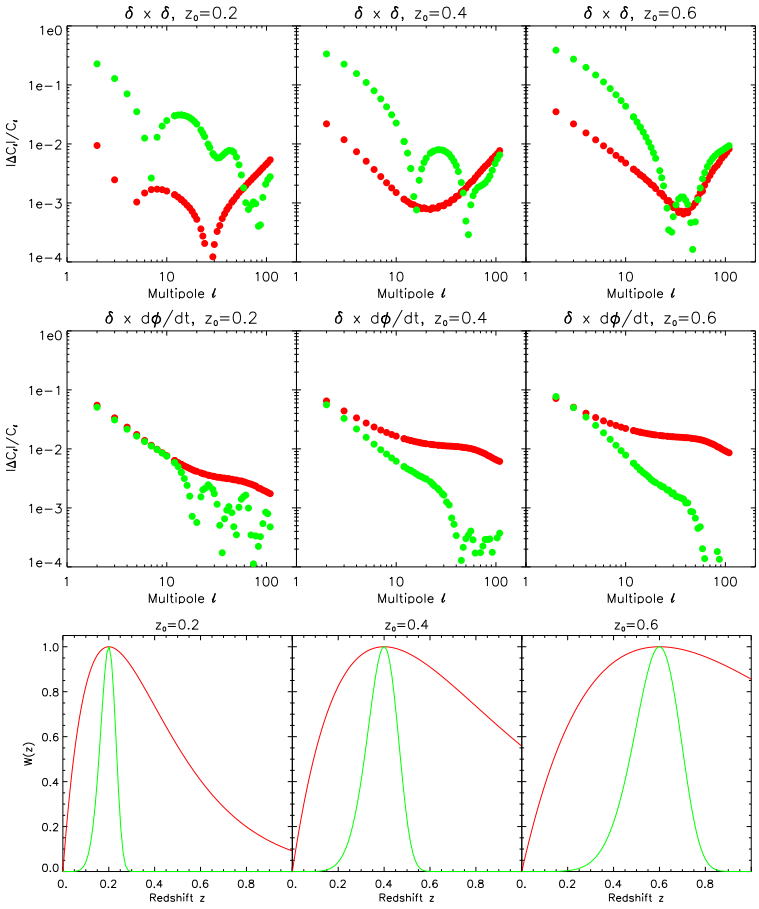

FIG. 19: Comparison of the exact C_l evaluation for the ISW–density tracer correlation with the Limber approximation evaluation. The top three panels show the relative errors for a near, intermediate and far density tracer survey. Solid lines denote predictions for thick redshift shell and dash lines denote thin redshift shells. The corresponding bottom panels show the redshift distributions.